Geometric Investigation of Association/Dissociation Kinetics with an Application to the Master Equation for CH$_3$ + CH$_3$ ↔ C$_2$H$_6$

Michael J. Davis*,† and Stephen J. Klippenstein‡

*Chemistry Division, Argonne National Laboratory, Argonne, Illinois 60439, and
Combustion Research Facility, Sandia National Laboratories, Livermore, California 94551-0969*

Received: November 12, 2001; In Final Form: March 19, 2002

The dynamics of association/dissociation kinetics is studied, with an application to the titled reaction. The focus is the geometry of the phase space of the phenomenological rate law, a Lindemann mechanism, and the master equation of this reversible reaction, all of which are nonlinear. It is shown that all three systems possess similar phase space structure, including a 1-D manifold. This 1-D manifold describes asymptotic motion for either dissociation or recombination and is the analogue of the corresponding eigenvector for linear master equations describing dissociation without recombination. The 1-D manifold allows for the separation of asymptotic motion from transient behavior and together with other manifolds in phase space allows a better understanding of the dissociation and recombination processes. The 1-D manifold also allows us to test various approximations that have been used in the past to calculate association rate constants from the master equation and Lindemann mechanism and develop new methods for calculating association rate constants and generating rate laws.

I. Introduction

For the last few decades, master equations have been used to extract pressure-dependent unimolecular dissociation rate constants, with refs 1 and 2 providing summaries of work done by many researchers. More recently, the uses of master equations have been extended beyond unimolecular reactions, including association reactions, bimolecular reactions, and multiple well/multiple channel reactions.[3−16] Many of these cases include nonlinearity, differing from the unimolecular case, which is linear. There, matrix diagonalization can be used to extract asymptotic rates and thus rate constants. For nonlinear master equations, approximations often need to be used to calculate rate constants. Generally, these approximation are good but are not always tested thoroughly.

In this paper, we present results from the study of one type of nonlinear master equation, the one describing association and dissociation. In a previous paper by one of us and Harding,[17] pressure-dependent rate constants for methyl recombination were calculated using the Variflex program.[18] The main focus of ref 17 was the incorporation of good information concerning potential energy surface features and statistical reaction theory as well as comparison with experiments rather than the details of the master equation calculation. In this paper, we look in more detail at the dynamics of the master equation.

Another reason for the investigation undertaken here is the recent work of one of us[19−21] and others[22−27] on the asymptotic dynamics of kinetic equations. Until recently,[20,28] these techniques were applied only to complex chemical kinetics, although there is a history of more rigorous approaches (i.e., beyond steady-state approximations) used to model master equations.[29−33] The techniques used in refs 19−28 involve the calculation of low-dimensional manifolds that describe the asymptotic dynamics of systems approaching equilibrium and are more rigorous than the steady-state approximation. For nonlinear master equations, a low-dimensional manifold is analogous to the eigenvector with least negative eigenvalue,[20] the one used to calculate a pressure-dependent unimolecular rate constant.[1,2] In addition, low-dimensional manifolds allow for the systematic elucidation of the global phase space structure of a dynamical system that approaches an equilibrium point at long time.[19] The elucidation of the phase space structure allows for a better understanding of transient effects.

This paper will lay out a plan of attack for studying both the long-time dynamics and the transients of the association/dissociation master equation and the related Lindemann mechanism. Previous work on such systems has generally ignored the nonlinearity or incorporated it in an approximate way. One of the purposes of this paper is to suggest ways to study the nonlinear system and calculate rate constants with the nonlinearity fully included.

The outline of this paper is as follows. Section II is a study of the dynamics of the phenomenological rate law from a geometric standpoint. Section III addresses similar issues for the Lindemann mechanism and investigates ways to extract rate constants. Section IV applies what has been learned in the previous two sections to the dynamics of a master equation describing the reversible reaction in the title. It is shown that association rate constants can be extracted in a novel way, but it demonstrates that this extraction leads to rate constants that vary with position in phase space. Section V presents a more general and difficult procedure to generate rate laws and demonstrates that the notion of an equilibrium constant may break down along a 1-D manifold. Section VI has further discussion and a conclusion.

II. Background: The Phenomenological Rate Law

Many of the tools used in the rest of the paper can be developed for the phenomenological rate law of the reversible reaction

$$A + A + M \leftrightarrow C + M \qquad (2.1)$$

* Corresponding author. E-mail: davis@tcg.anl.gov.
† Argonne National Laboratory.
‡ Sandia National Laboratories.

Association/Dissociation Kinetics

J. Phys. Chem. A, Vol. 106, No. 24, 2002 **5861**

where the reactive species are A and C and M is a third body, which leads to pressure dependence. The two directions are characterized by the forward association rate constant, k_a, and the reverse dissociation rate constant, k_d. These rate constants are temperature- and pressure-dependent.

A. Rate Equations and Constants of the Motion. For methyl recombination with possible subsequent dissociation of ethane to two methyl radicals, eq 2.1 becomes

$$CH_3 + CH_3 \xrightarrow{k_a} C_2H_6 \qquad (2.2a)$$

$$C_2H_6 \xrightarrow{k_d} CH_3 + CH_3 \qquad (2.2b)$$
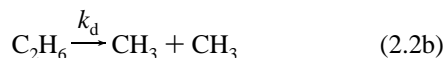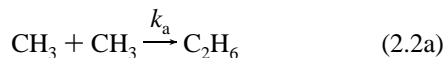
where the third body M has been dropped. The rate law for this system is[34]

$$\frac{d[C_2H_6]}{dt} = -k_d[C_2H_6] + k_a[CH_3]^2 \qquad (2.3a)$$

$$\frac{d[CH_3]}{dt} = 2k_d[C_2H_6] - 2k_a[CH_3]^2 \qquad (2.3b)$$

where the brackets indicate concentration. Because of conservation of mass (which can be checked by adding the equations), there is a constant of the motion

$$c = 2[C_2H_6] + [CH_3] \qquad (2.4)$$

This constant reduces the 2-D system of eq 2.3 to a 1-D system and allows for an analytical expression for the time development of the two species.[34] For the case in eq 2.1 where A + B replaces A + A, this constant changes in an obvious way, and there is an additional constant, [A] − [B].

By scaling the concentrations and using the constant defined in eq 2.4, the rate law for methyl is

$$\dot{y} = k_d(1 - y) - 2k_a c y^2 \qquad (2.5a)$$

$$x \equiv \frac{[C_2H_6]}{c} \qquad y \equiv \frac{[CH_3]}{c} \qquad 2x + y = 1 \quad (2.5b)$$

reducing it to a 1-D dynamical system.

B. Dynamics. Equation 2.5a can be integrated for the time development of the methyl radical[34] and in turn for ethane through the constant in eq 2.4:

$$y = \sqrt{\frac{K_{eq}}{2c} + \frac{K_{eq}^2}{16c^2}\left(\frac{re^{\rho t} - 1}{re^{\rho t} + 1}\right)} - \frac{K_{eq}}{4c} \qquad K_{eq} = \frac{k_d}{k_a} \quad (2.6a)$$

$$r = \frac{\sqrt{\dfrac{K_{eq}}{2c} + \dfrac{K_{eq}^2}{16c^2}} + \dfrac{K_{eq}}{4c} + y_0}{\sqrt{\dfrac{K_{eq}}{2c} + \dfrac{K_{eq}^2}{16c^2}} - \dfrac{K_{eq}}{4c} - y_0} \qquad (2.6b)$$

with

$$\rho = 2\sqrt{2k_d k_a c + \frac{k_d^2}{4}}$$

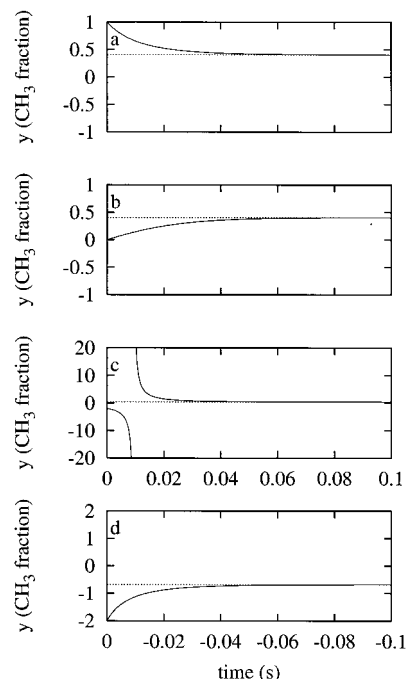y_0 is the initial value of y. Equation 2.6 demonstrates that at

Figure 1. Trajectories shown for eq 2.6a with rate constants calculated in section IVC at $T = 1350$, $P = 1000$ Torr, $\Delta E_d = 200$ cm^{-1}, and $c = 1 \times 10^{13}$ molecules/cm^3. The two rate constants are $k_a = 2.96 \times 10^{-12}$ cm^3/s and $k_d = 16.355$ s^{-1}. The top three trajectories are forward propagated and the bottom, backward propagated.

long time all trajectories except one approach the equilibrium point

$$y_{eq} = \frac{1}{c}\left(\frac{-K_{eq}}{4} + \sqrt{\frac{K_{eq}^2}{16} + \frac{K_{eq}c}{2}}\right) \qquad (2.7)$$

The exceptional point is for $r = 0$ (eq 2.6b)

$$y_s = \frac{1}{c}\left(\frac{-K_{eq}}{4} - \sqrt{\frac{K_{eq}^2}{16} + \frac{K_{eq}c}{2}}\right) \qquad (2.8)$$

where the designation "s" is for source and is described in the next subsection. Except for the equilibrium point, all trajectories that are run backward in time approach this point.

To ensure that the concentrations of methyl and ethane are positive, $0 < y < 1$. Equation 2.6 demonstrates that trajectories initiated in this physically allowed region always remain in it. For comparison to observables, it is necessary to examine the dynamics in this region only. However, to obtain a global picture of the dynamics and to generate asymptotic (in time) results for the physical region, it is useful to extend the analysis beyond the physical region.[19] Equation 2.6 demonstrates that in the nonphysical region there is a singularity, so trajectories started with y values less than that of the source point approach $-\infty$ and switch branches to approach the equilibrium point from the positive side.

Figure 1 shows several trajectories for eq 2.6. These are generated for eq 2.2 at $T = 1350$ K and $P = 1000$ Torr, with c (eq 2.4) set to 1×10^{13} molecules/cm^3. The rate constants were calculated for $\Delta E_d = 200$ cm^{-1} (section IVC). The top three panels of Figure 1 show trajectories propagated forward in time. Two of these (Figures 1a and b) are started in the physically allowed region and one is started in the nonphysical region (Figure 1c). This latter trajectory is started on the negative side of the source and moves through the singularity. These

trajectories approach the equilibrium point at long time, as indicated by the dotted line in the panels. Some trajectories, such as those between the two fixed points, approach from the methyl-rich region (y values greater than the equilibrium value, Figure 1a), and others (Figure 1b) approach from the methyl-poor region (y values less than the equilibrium value). Figure 1d shows a trajectory that is run backward in time and approaches the source (dotted line) as $t \rightarrow -\infty$.

C. Global Phase Space Dynamics. The first step in generating the global phase space structure is to find the fixed points.[35] These were described in eqs 2.6b and 2.7. In general, dynamical systems cannot be integrated in closed form as in the previous subsection, but fixed points can still be found. For the scaled version of the phenomenological rate law, the fixed points are found by setting eq 2.5a to zero (when the time derivative is zero at any point the trajectory is "fixed" at the point)

$$0 = k_d (1 - y) - 2k_a c y^2 \qquad (2.9)$$

and the two fixed points are obtained as the two roots of this equation. At equilibrium or at the source, $y^2/x = K_{eq}$ as expected. The nature of the two fixed points (equilibrium or source) is judged as such from the linearization of eq 2.5a,

$$\frac{d\dot{y}}{dy} = - k_d - 4k_a c y \qquad (2.10)$$

When $y > 0$, this quantity is negative and thus the equilibrium point is attractive. When $y < -K_{eq}/4$, the right side of eq 2.10 is positive, and this identifies the source as repulsive. To investigate the global dynamics, it is useful to examine the dynamics out to infinity. The following coordinates are introduced:[35]

$$u = \frac{y}{\sqrt{1 + y^2}} \qquad (2.11)$$

$$v = \frac{1}{\sqrt{1 + y^2}}$$

Although this transformation adds a dimension, the coordinates are restricted to the positive v portion of a unit circle, which means motion is still 1-D. Infinity in the Cartesian coordinate system is located at $v = 0$ in this coordinate system.

Figure 2 summarizes the global dynamics for the rate law of eq 2.5a as well as the two limiting cases of first-order and second-order kinetics, as indicated on each plot. Each plot has fixed points marked on them as large dots. In each of the top two panels, there is a single finite fixed point compared to the two fixed points in the bottom panel (eq 2.9). In addition, first-order kinetics (top panel) has two sources at infinity. These result from the blow-up of the differential equations backward in time. The bottom panel of Figure 2 shows arrows that point to the four trajectories of Figure 1. Because of the original scaling of coordinates to give x and y, the physical region in Figure 2 is $0.0 \leq u \leq 1/\sqrt{2}$. Figure 2 presents generic dynamical behavior for the indicated kinetic systems. As the parameters change (for example, c and the rate constants), the locations of the finite fixed points as well as the time scales change, but the dynamical flow is not altered.

Figures 1 and 2 show how a global analysis is useful. The behavior of the several forward-moving trajectories of Figures 1a−c can be summarized with a single plot. The behavior of trajectories run backward in time (Figure 1d) can be summarized
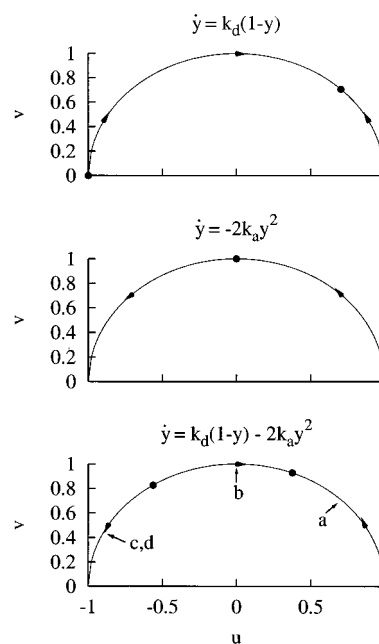

Figure 2. Global phase-space portrait of the system in Figure 1 shown along with the contrasting portraits for first- and second-order kinetics in the top and middle panels.

with plots such as those in Figure 2 merely by switching the direction of the arrows.

III. Lindemann Mechanism

The Lindemann mechanism[1,2] is the next level of complexity beyond the rate law of the previous section and has most of the important dynamics of the master equation, possessing additional features compared to the rate law of the previous section. Although the Lindemann mechanism is generally used to model the pressure dependence of unimolecular decomposition, it is straightforward to add association. In this form, it is still a 2-D system, and it possesses an easily identified reduction to a 1-D manifold. Like the master equation, it is nonlinear.

A. Rate Equations and Constants of the Motion. The Lindemann mechanism for the reaction in eq 2.1 is

$$A + A + M \leftrightarrow C^* + M \qquad (3.1a)$$

$$C^* + M \leftrightarrow C + M \qquad (3.1b)$$
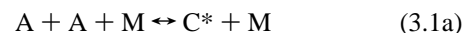
In master equations for a system of this form, the molecule C is modeled with a series of states, and the energy transfer process in eq 3.1b is modeled by a series of transitions between states (see refs 1 and 2 and the next section). Therefore, we consider the Lindemann mechanism a two-state version of the master equation with unexcited C considered to be state one and C*, state two. The following rate law results:

$$\frac{dx_1}{dt} = -a_{11}x_1 + a_{12}x_2 \qquad (3.2a)$$

$$\frac{dx_2}{dt} = a_{21}x_1 - a_{22}x_2 - kx_2 + k_a c y^2 \qquad (3.2b)$$

$$\frac{dy}{dt} = 2kx_2 - 2k_a c y^2 \qquad (3.2c)$$

Once again, there is a constant:

$$c = 2([C] + [C^*]) + [A] \qquad (3.3)$$

Association/Dissociation Kinetics

J. Phys. Chem. A, Vol. 106, No. 24, 2002 **5863**

The variables x_1, x_2, and y are scaled versions of the concentrations, as they were in eq 2.5, with x_1, x_2, and y the scaled versions of [C], [C*], and [A], respectively. Because of c, eq 3.2 can be reduced to a 2-D system

$$\frac{dx_1}{dt} = -a_1 x_1 + a_2 x_2 \qquad (3.4a)$$

$$\frac{dx_2}{dt} = a_1 x_1 - (a_2 + k)x_2 + k_a c(1 - 2x_1 - 2x_2)^2 \qquad (3.4b)$$

$$a_1 = af_2, \qquad a_2 = af_1, \qquad f_1 + f_2 = 1 \qquad (3.4c)$$

where microscopic reversibility has been invoked[1,2] (the system relaxes to a Boltzmann distribution at long time, with f_1 and f_2 the equilibrium populations). The derivation of a is described below and in the Appendix. Conservation of probability for the closed system has also been included (the sum of eqs 3.4a and 3.4b is zero when k and k_a are zero).

The Jacobian of the system is[35]

$$J = \begin{pmatrix} -af_2 & af_1 \\ af_2 - 4k_a cy & -(af_1 + k) - 4k_a cy \end{pmatrix} \qquad (3.5)$$

J describes the local linearized dynamics near a point and depends only on y. This Jacobian is the 2-D version of eq 2.10. It can be used to calculate the stability of fixed points.

The eigenvalues of J are

$$\lambda_{\pm} = -\frac{1}{2}[a + k + 4k_a cy \pm$$
$$\sqrt{(a + k + 4k_a cy)^2 - 4a(4k_a cy + kf_2)}] \qquad (3.6)$$

The square root in eq 3.6 can be expanded in terms of

$$\frac{4a(4k_a cy + kf_2)}{(a + k + 4k_a cy)^2} \qquad (3.7)$$

which is very small for most values of the parameters (see the Appendix and the caption to Figure 3) because the expression in the parenthesis of the numerator is much smaller than a and k. An expansion and algebraic manipulation gives the following eigenvalues:

$$\lambda_1 = -\frac{a(4k_a cy + kf_2)}{a + k + 4k_a cy} + \ldots \qquad (3.8a)$$

$$\lambda_2 = -(a + k + 4k_a cy) + \frac{a(4k_a cy + kf_2)}{a + k + 4k_a cy} + \ldots \qquad (3.8b)$$

In the physical region, both eigenvalues are negative under chemical kinetics conditions, with λ_1 much lower in magnitude than λ_2, and the one associated with the rate constants for association and dissociation.[1,2] The first term on the right-hand side of eq 3.8b dominates under most conditions, and because $(a + k) \gg 4k_a cy$ under these conditions, λ_2 is nearly constant. For the same reason, λ_1 is generally a linear function of y.

The eigenvectors of the Jacobian in the (x_1, y) plane are

$$y = \frac{-2(a + \lambda_1)}{af_1} x_1 + b \cong \frac{-2}{f_1} x_1 + b \qquad a \gg \lambda_1 \qquad (3.9a)$$

$$y = \frac{k + 4k_a cy_0 - \lambda_1}{af_1} x_1 + b \cong \frac{k}{af_1} x_1 + b \qquad k \gg 4k_a cy_0, \lambda_1 \qquad (3.9b)$$
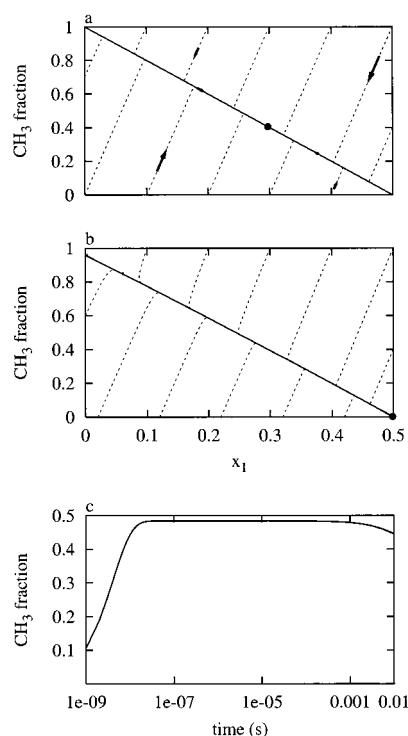

Figure 3. Some trajectories for the Lindemann mechanism (eq 3.4) with different values of c shown in the top two panels and the time development of one shown in the bottom panel. This trajectory is the one started at (0.2, 0.0) in Figure 3a. The Lindemann parameters were derived as described in the Appendix for the master equation at $T = 1350$ K, $P = 1000$ Torr, $\Delta E_d = 200$ cm^{-1}, and $c = 1 \times 10^{13}$ molecules/cm^3. These parameters are $a = 4.75 \times 10^7$ s^{-1}, $k = 1.98 \times 10^8$ s^{-1}, and $f_2 = 4.26 \times 10^{-7}$ with $c = 1 \times 10^{13}$ and 3.5×10^{17} cm^{-1} in panels a and b, respectively.

where y_0 refers to the point where the Jacobian is evaluated and b refers to the intercept of the line, which is calculated from the equilibrium point. Equation 3.9a describes the eigenvector for λ_1 and eq 3.9b, for λ_2.

B. Global Dynamics: Fixed Points, Low-Dimensional Manifolds, and Basins. Figures 3a and b show several trajectories for a set of parameters extracted from the master equation of section IV (see the Appendix). Figure 3 shows the scaled CH$_3$ variable (y) versus unexcited C$_2$H$_6$ (x_1), with Figure 3a showing results for a density parameter c (eq 3.3) of 1×10^{13} molecules/cm^3 and Figure 3b showing results for $c = 3.5 \times 10^{17}$ molecules/cm^3. Trajectories are drawn as dashed lines in Figures 3a and b except for one trajectory that is shown as a thicker solid line. The equilibrium point for each system is shown as a large dot on each of the panels. The direction of flow for some of the trajectories is shown in Figure 3a. A time profile of one of the trajectories of Figure 3a is shown in Figure 3c (the trajectory starts at (0.2, 0.0) in Figure 3a).

The top two panels of Figure 3 show that trajectories reach a well-defined 1-D curve, and Figure 3c demonstrates that trajectories do so in a short time followed by a slow approach to the equilibrium point along this manifold. Figure 3c shows that a typical trajectory takes between 10 and 100 ns to reach the manifold and tens of milliseconds to get close to equilibrium. The time scales decrease as the density of reactive species increases.

To better understand the nature of trajectories for the Lindemann mechanism, it is useful to generate a global picture of the dynamics. The first step, once again, is to find the fixed points. This is done by setting the velocities in eqs 3.4a and

3.4b to zero (the left-hand sides). Equation 3.4a can have a nontrivial zero (i.e., $x_1 \neq 0$ and $x_2 \neq 0$) only when x_1 and x_2 are the same fraction of their equilibrium values f_1 and f_2, respectively, giving

$$0 = \gamma a(-f_2 f_1 + f_1 f_2) \tag{3.10a}$$

$$0 = -k\gamma f_2 + k_a c(1 - 2\gamma)^2 \tag{3.10b}$$

Equation 3.10a is satisfied, and eq 3.10b gives the following two fixed points:

$$x_1 = \gamma_\pm f_1, \quad x_2 = \gamma_\pm f_2, \quad \gamma_\pm = \frac{1}{c}\left(\frac{K_{eq} + 4c}{8} \pm \sqrt{\frac{K_{eq}^2}{64} + \frac{cK_{eq}}{8}}\right) \tag{3.11a}$$

$$y = \frac{1}{c}\left(\frac{-K_{eq}}{4} \mp \sqrt{\frac{K_{eq}^2}{16} + \frac{cK_{eq}}{2}}\right) \tag{3.11b}$$

Equation 3.11b is identical to eqs 2.7 and 2.8. One of the fixed points here is the equilibrium point (two negative eigenvalues)

$$x_{1,eq} = \gamma_- f_1, \quad x_{2,eq} = \gamma_- f_2, \quad y_{eq} = \frac{1}{c}\left(\frac{-K_{eq}}{4} + \sqrt{\frac{K_{eq}^2}{16} + \frac{cK_{eq}}{2}}\right) \tag{3.12}$$

The other point is a saddle point (one positive, one negative).

Associated with each fixed point are stable and unstable manifolds[35] (see also ref 19). One type of manifold is shown in Figures 3a and b with a thick line. This is a stable manifold for the equilibrium point and is commonly called the slow manifold[22] because it is the direction of final approach to equilibrium, as demonstrated in Figure 3. The nature of the manifolds leads to a global understanding of the dynamics,[35] and this is demonstrated in Figure 4 for the parameters of Figures 3a and b. These are plotted in the coordinates of eq 2.11, which are defined for the Lindemann mechanism as

$$u_1 = \frac{x_1}{\sqrt{1 + x_1^2 + y^2}} \tag{3.13a}$$

$$u_3 = \frac{y}{\sqrt{1 + x_1^2 + y^2}} \tag{3.13b}$$

$$v = \frac{1}{\sqrt{1 + x_1^2 + y^2}} \tag{3.13c}$$

Any pair of coordinates can be used. Once again, as in section IIC, there is an additional dimension, but trajectories move on the surface of a sphere in 3-D space, which renders the dynamics 2-D. The dynamics, which can be projected onto a plane, fills a circle of radius = 1, with infinity in the original coordinates corresponding to the circumference of the circle.

Fixed points are shown as solid dots in Figure 4. Besides the two finite fixed points discussed above, there are four "fixed points at infinity".[35] The slow manifold is plotted as a thick solid line, and trajectories (dashed lines) approach this curve on their way to equilibrium or the fixed point at (0.0, 1.0), which is another sink. The thinner solid line is a manifold from the saddle run backward in time and is the boundary between trajectories that are asymptotic to the equilibrium and the sink at infinity. At the saddle point, this manifold corresponds to the eigenvector for the negative eigenvalue. Figure 4a also
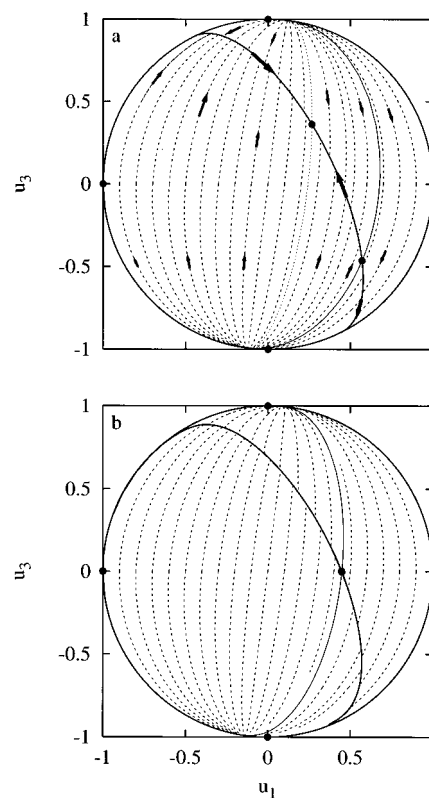

Figure 4. Global phase-space portraits for the systems of Figures 3a and b. All trajectories in a basin go to the relevant sink, the dominant one being the equilibrium point at (0.27, 0.36) in Figure 4a. The arrows on the top panel indicate the direction of the flow. The dotted curve divides the equilibrium basin into associative and dissociative trajectories. See text for further details.

includes arrows on some of the trajectories and the slow manifold, which indicate the direction of the flow. The slow manifold is also a trajectory that is started at infinity from either of two fixed points there. Figure 4a includes a dotted line that separates "dissociative" from "associative" trajectories. Dissociative trajectories are those that approach equilibrium from the ethane-rich end (u_1 values greater than the equilibrium value of u_1), and associative trajectories are those that approach from the methyl-rich end. Because c is higher in Figure 4b, dissociation is favored (Figure 3b), and the saddle point lies almost on top of the equilibrium point, masking some of the features. For example, the dotted line that separates associative from dissociative trajectories cannot be observed on the scale of Figure 4b

Figure 5 makes this discussion clearer for Figure 4a. All the lines have the same meaning as they do in Figure 4. The arrows show the direction of the approach to equilibrium. The thinner solid line is, along with the circular boundary, the "basin boundary". All trajectories inside this region approach the equilibrium point at long time along the slow manifold. Trajectories outside this region move to the sink at infinity. The dotted line in Figure 5 divides the basin into two parts, as described in the bottom two panels. The middle panel shows that all trajectories in the region to the right of the equilibrium point are dissociative, and the bottom panel shows that those to the left are associative.

C. Transient and Asymptotic Behavior: Pressure, Density, and Temperature Dependence. Equations 3.2 and 3.4 show an explicit dependence on the density of reactive species but no explicit dependence on pressure. Pressure dependence is part of the parameter a, which also depends on temperature. There

Association/Dissociation Kinetics
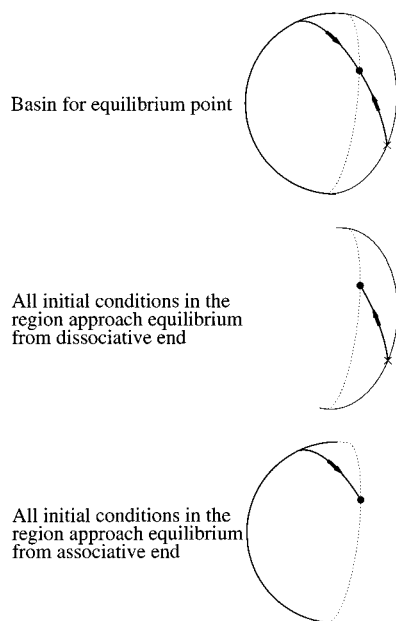
J. Phys. Chem. A, Vol. 106, No. 24, 2002 **5865**

Figure 5. These plots elucidate the phase-space structure of Figure 4a.

is also a temperature dependence in the infinite pressure association rate constant k_a. It is well-known that a is linearly dependent on pressure,[1,2] and therefore a can be defined as

$$a = Pa'(T) \tag{3.14}$$

$a'(T)$ depends on temperature through the collision rate.

Figure 6 shows the way asymptotic and transient behavior changes with pressure and density for a specific temperature. The three columns in this Figure correspond to three densities, c, as noted there. The three rows correspond to three pressures: 100, 1000, and 10 000 Torr. The parameters of the Lindemann mechanism for the middle plot ($c = 1 \times 10^{13}$ and $P = 1000$ Torr) were generated from a fit to the master equation data (see the Appendix). The other parameters in the Figure were calculated by scaling a (eq 3.14) up or down by a factor of 10 and by adjusting c in eqs 3.2 and 3.4.

The plots in Figure 6 include a solid, thick line showing the slow manifold, which is nearly linear. The slow manifold is also nearly the boundary for the physically realizable region of the phase plane, which has the equation $y = 1 - 2x_1$. Anything above this line means that $x_2 < 0$. Also included on each plot are three open circles indicating three initial trajectories to focus the discussion of transients. The open circles at (0.0, 1.0) and (0.5, 0.0) are initial conditions with pure methyl or unexcited ethane, respectively, which would be the most common experimental initial conditions. The open circle at (0.0, 0.0) indicates pure excited ethane ($x_2 = 0.5$). The solid dots show the equilibrium points.

The equilibrium points change with c along any row but have no pressure dependence. The slow manifold does not appear to change with either pressure or density, a result not assured by anything discussed previously, although eq 3.9a shows that the eigenvector for λ_1 has a very weak dependence on pressure and density. The slow manifold lines up along the eigenvector near equilibrium,[35] which is consistent with its lack of dependence on pressure or density.

All plots in Figure 6 include the fast manifold as a dotted line. One of these was already shown in Figures 4 and 5. This manifold is generated by running a trajectory that started on the eigenvector for λ_2 near the equilibrium point backward in

time. Like the slow manifold, the fast manifold does not deviate in any noticeable way from the eigenvector in any of the plots. However, the fast manifold is dependent on pressure, as indicated in eq 3.9b, because it has an inverse dependence on a.

All panels in Figure 6 show the behavior of the three trajectories, but only the trajectory started at (0, 0) and plotted as a dashed line exhibits transient behavior because the other two lie almost exactly on the slow manifold. The asymptotic behavior of this trajectory is determined by what side of the fast manifold it lies on compared to the position of the equilibrium point. When the initial condition lies on the ethane-rich side of the fast manifold, it reaches the slow manifold, and then the ethane shows enhanced dissociation. When the initial condition lies on the ethane-poor side of the fast manifold, the trajectory reaches the slow manifold and then exhibits enhanced association.

Figure 7 shows the time development of the three dashed trajectories in the middle row of Figure 6, with the top-to-bottom panels in Figure 7 corresponding to the left-to-right panels in the middle row of Figure 6. Figure 7 demonstrates that the long time scales tend to decrease with increasing c, but the short time scales remain about the same. The effect described in the previous paragraph is evident in Figures 6 and 7. For example, the first panel of the middle row of Figure 6 shows that the trajectory started at (0, 0) lies on the ethane-rich side of equilibrium. The fast manifold in the middle row indicates that as trajectories approach the slow manifold there is an increase in unexcited ethane (x_1) and methyl. After reaching the slow manifold, there is a time period over which the system exhibits a slow increase (Figure 7a) in the methyl fraction as ethane dissociates. In the other two panels of the middle row of Figure 6, the trajectory lies on the ethane-poor side of the fast manifold. In these cases, the trajectories reach the slow manifold and then show slow dissociation of ethane.

The behavior exhibited in Figures 6 and 7 quantifies chemical intuition for the Lindemann mechanism. At low pressure, excited ethane tends to dissociate before the steady state sets in and then takes a long time to reequilibrate, meaning the association of methyl radicals to ethane and final equilibrium. At higher pressures, there is enough buffer gas to relax the excited ethane, and then the slow step is redissociation to form a final equilibrium with a mixture of unexcited ethane (x_1), excited ethane (x_2), and methyl radical.

Figures 6 and 7 display results for the Lindemann mechanism that are common over large pressure, density, and temperature ranges. There is little visible effect of the nonlinearity nor is there much transient behavior for pure, unexcited ethane ($x_1 = 0.5$) or pure initial methyl ($y = 1.0$). However, there are some situations where transients are noticeable for both of these types of initial conditions, and Figure 8 shows two cases.

The top panel of Figure 8 shows the result for $P = 10\,000$ Torr, with an initial density of methyl of 3.5×10^{18} molecule/cm^3 or 5% dilution of methyl in argon buffer gas. The solid line shows the slow manifold, which is now curved because the nonlinear term in eq 3.2b is similar in magnitude to the linear terms. The slow manifold still lines up with the appropriate eigenvector near the equilibrium point (eq 3.9a), but it curves away from it as the methyl fraction (y) increases. This leads to transient behavior where the pure methyl initial condition on the top panel (0.0, 1.0) is now started off the manifold and merges with the manifold near (0.15, 0.62) after approximately 8 ns. Because the slow manifold is generated with the methods reported in ref 19, it does not matter whether the manifold is
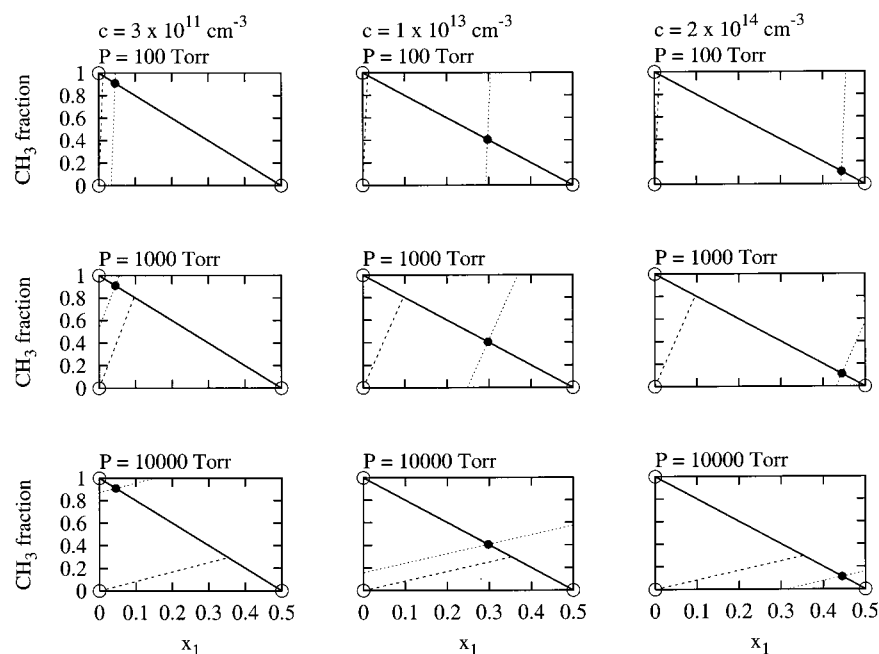
Figure 6. Series of plots showing how the phase-space structure changes with pressure and c. These changes affect the behavior of transients. Initial conditions are open circles, and dashed lines are trajectories started there. The parameters are the same as those in Figures 3−5, with the quantities c and a changed to reflect density and pressure changes (see the Appendix).
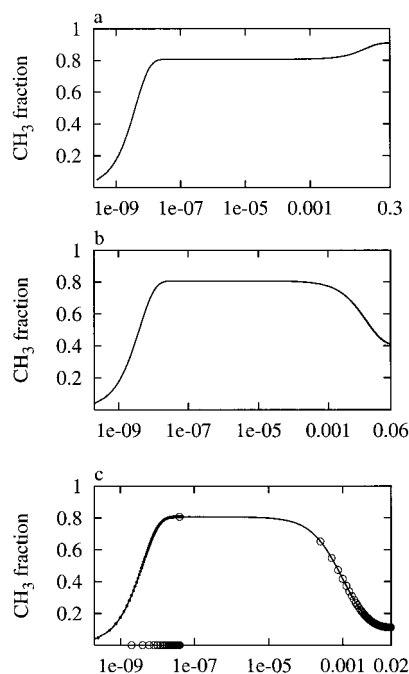

Figure 7. Time dependence of the three dashed trajectories of the middle row of Figure 6 shown from top to bottom versus left to right in Figure 6. The open circles show the time behavior of the phenomenological rate law for the initial condition started at (0, 0) in Figure 6. At short times, it is inaccurate, but it is accurate at long times. Compare this behavior to that of the trajectory started at (0.5, 0.0), which is accurate at short time (dots).

linear or whether the manifold conforms to the steady-state approximation, although the latter condition is attained in this case (see next subsection). The transient shown in the top panel of Figure 8 is rapid and less common than it is for the master equation of the next section.

A more unusual case of transient behavior for the Lindemann mechanism is pictured in the bottom panel of Figure 8. It is difficult to observe transitions from unexcited to excited ethane
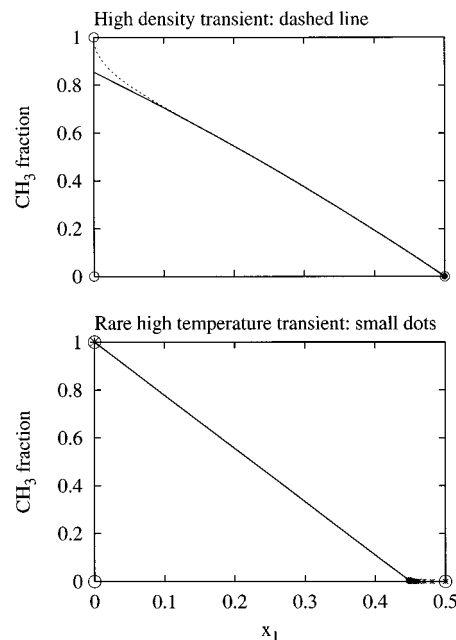

Figure 8. Situations where transients occur for initial conditions that are pure methyl (top plot) and pure unexcited ethane ($x_1 = 0.5$). When the density is high enough, the first case occurs, and at high temperature, the second case occurs (bottom plot).

for the Lindemann mechanism for the temperature range studied in ref 17 because the equilibrium populations of excited ethane are very much lower than those for unexcited ethane and the ratio of up to down transitions is the ratio of these two quantities (eq 3.4). In the bottom plot of Figure 8, the temperature has been raised ($f_1 = 0.9, f_2 = 0.1$), and the density has been lowered to 1×10^{10} molecules/cm^3 compared to the middle row of Figure 6, leading to transient behavior for the pure unexcited ethane initial condition. Dots show the trajectory, which merges with the slow manifold near (0.45, 0.0) after approximately 0.1 μs.

Association/Dissociation Kinetics

J. Phys. Chem. A, Vol. 106, No. 24, 2002 **5867**

D. Low-Dimensional Manifolds and the Steady-State Approximation. In the Lindemann mechanism for unimolecular dissociation, the steady-state approximation is invoked for the excited molecule to generate a 1-D system and extract a pressure-dependent rate constant.[36] This is done even though the kinetics is linear and the appropriate rate constants can be extracted from the diagonalization of a 2×2 matrix, which has an analytical form similar to that of eqs 3.6–3.8. It is recognized that the rate constant is more complicated when represented this way, and because of the vast difference between the rate of relaxation downward (a_2 in eq 3.4) versus upward (a_1), the steady-state approximation is very accurate.[37] Although there are extra terms in the Lindemann mechanism of eqs 3.2 because of the association terms, the steady-state approximation is still very accurate.

The steady-state approximation is found by setting $dx_2/dt = 0$ in eq 3.4b. In the (x_1, y) plane, it has the following form:

$$x_1 = \frac{1}{a+k}\left[\frac{1}{2}(a_2+k)(1-y) - k_a cy^2\right] \quad (3.15)$$

Because the coefficient of the linear term is usually much larger than the coefficient of the quadratic term and because $0 < y < 1$ in the physically allowed region, the steady-state approximation is nearly linear except when c is high. Similar behavior is demonstrated in Figures 6 and 8a for the low-dimensional manifolds.

Figure 9a compares the steady state approximation to the 1-D manifold of the system studied in the middle row of Figure 6. Figure 9b compares to the high-density case in the upper plot of Figure 8. In each plot, the 1-D manifold is drawn with a solid line, and the steady state approximation is represented by a series of dots. In both cases, the steady-state approximation is nearly exact, even in the high-density case (Figure 8a) where the low-dimensional manifold is curved in the physically allowed region. Small differences can be observed for this latter case when the comparison is made in a plane including excited ethane (x_2), which has very low values along the manifold.

A case where the steady-state approximation is noticeably different than the low-dimensional manifold is shown in the bottom panel of Figure 9. The parameters were generated from a master equation at $T = 474$ and $P = 1000$ Torr with $c = 4 \times 10^{18}$ molecules/cm^3 (see the Appendix). In the bottom panel of Figure 9, the 1-D manifold is plotted as a thick curved line, and the steady-state approximation, as a dotted line, with trajectories shown with dashed lines. The boundary of the physical region is a solid, straight line. The bottom plot of Figure 9 demonstrates that the low-dimensional manifold is a better representation of the asymptotic dynamics. The situation in the bottom panel of Figure 9 is rare for typical parameters of the Lindemann mechanism, but it is more common for the master equation, where there are many bins and the steady-state approximation can be defined in many ways depending on which bins are assumed to be in steady state.

E. Extracting Rate Constants. The traditional way to extract rate constants from a Lindemann mechanism is to invoke the steady-state approximation for x_2 and compare the resulting expression to the phenomenological rate law. This is accomplished by first inserting the steady-state expression in eq 3.15 to get the following expression for the rate of change of y

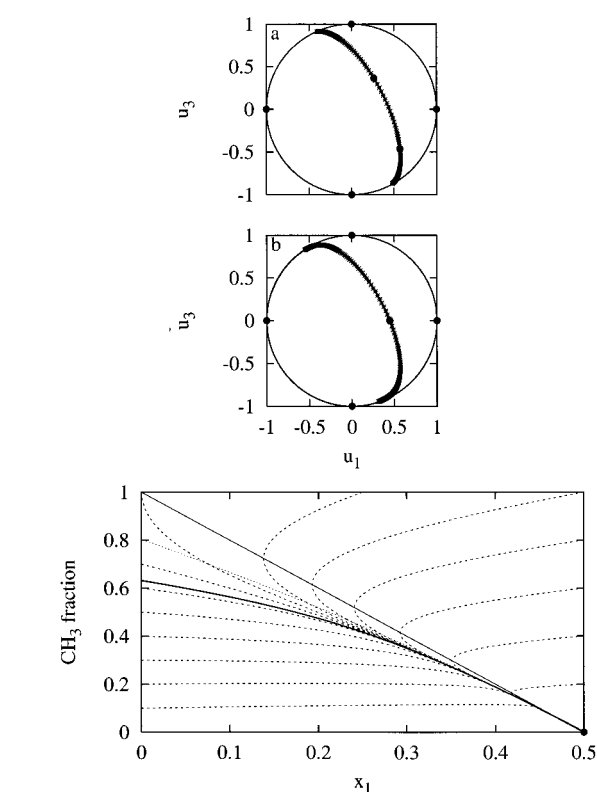$$\frac{dy}{dt} = \frac{akf_2}{a+k}(1-y) - \frac{2ak_a cy^2}{a+k} \quad (3.16)$$

Figure 9. Top two panels demonstrate the accuracy of the steady-state approximation. The parameters are the same as those of Figures 3a and b. The solid curved lines show the slow manifold, the small dots show the steady-state approximation, and the larger solid dots show the fixed points, with the one in the physical region being the equilibrium point. The steady-state approximation breaks down only under severe conditions. In the bottom panel, the thick solid line shows the slow manifold, and the dotted line shows the steady state approximation, with the solid thinner line showing the boundary of the physical region. The dashed lines are trajectories. The slow manifold is a better representation of the asymptotic dynamics, but trajectories are not attracted strongly to anything for x_1 values that are less than approximately 0.25, indicating that there is no good 1-D manifold in that region.

and then equating term-by-term with eq 3.2c to give

$$k_d = k_d^\infty\left(\frac{a}{a+k}\right) \quad (3.17a)$$

$$k_a = k_a^\infty\left(\frac{a}{a+k}\right) \quad (3.17b)$$

where k_a from the previous equations has been relabeled as k_a^∞ and $k_d^\infty \equiv kf_2$. Equations 3.18a and 3.18b are the standard expressions for the pressure dependence of the two rate constants.[1]

An alternate method for extracting the rate constants is by comparing the linearization in eq 2.10 with the smaller magnitude eigenvalue of eq 3.6:

$$k_a = \frac{-\lambda_1}{K_{eq} + 4cy} \quad (3.18)$$

Here, λ_1 is equated to $d\dot{y}/dy$ in eq 2.10. It is assumed that there is an equilibrium constant along the slow manifold, $K_{eq} = k_d/k_a$. The equilibrium constant is evaluated at the high-pressure limit. Equation 3.18 indicates that the rate constant is a function of the overall reactive density (c) and the fraction of density in the methyl radical (y). However, eq 3.8a shows that λ_1 is a
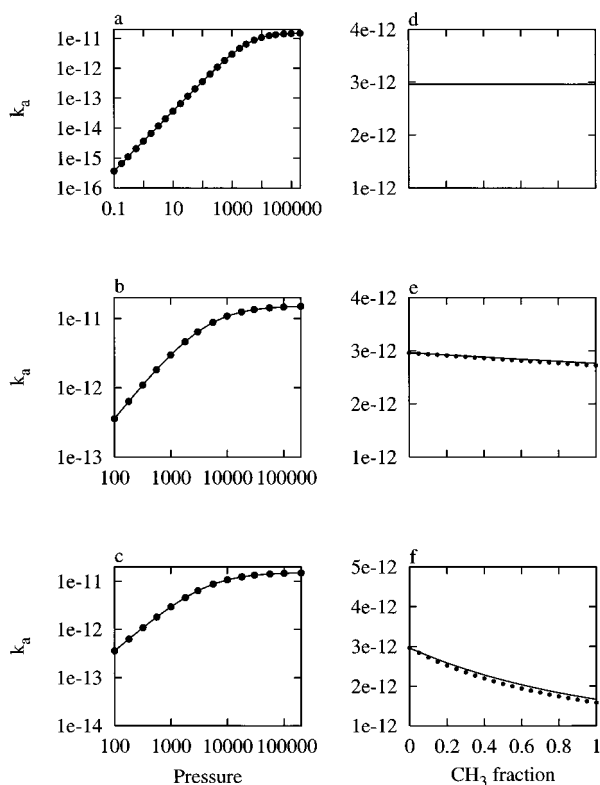
Figure 10. Association rate constants calculated at equilibrium vs pressure in Torr for the left column. The parameters are the same as those of Figure 3a except that the density constant, c, changes from top to bottom: (a) $c = 3 \times 10^{11}$ cm^{-3}, (b) 3.5×10^{17}, (c) 3.5×10^{18}. The solid lines in (a)−(c) show results for eq 3.18. The dots in the top and bottom panels of the column compare to the steady-state rate constants of eq 3.17b, and the dots in the middle panel compare to the results of the top panel. The association rate constant changes as a function of the methyl fraction, as shown in the right column. The panels correspond to the same parameters as Figure 3, with c fixed as in the left column of this figure. The dots in (e) and (f) were calculated with eq 3.19.

similar function of the same quantities. In the limit where the first term in the expansion of eq 3.8a is the accurate answer (which it is over a large range of parameters), the association rate constant is

$$k_a = \frac{a k_a^\infty}{a + k + 4 k_a^\infty c y} \quad (3.19)$$

where λ_1 of eq 3.8a has been substituted into eq 3.18. Except at high density, $4 k_a^\infty c y \ll a + k$, and eq 3.19 is equal to eq 3.17b. These equations are also equal at $y = 0$.

To calculate a rate constant from eq 3.18, a value of the methyl fraction (y) must be chosen. The natural choice is the equilibrium value, and the left column of Figure 10 shows the results of such a calculation. These plots are made at a series of densities (c), which are 3×10^{11}, 3.5×10^{17}, and 3.5×10^{18} molecules/cm^3 from top to bottom. The last density is unrealistically high, giving a 50% dilution of the reactive species in the buffer gas. The rate constants as a function of pressure are shown as solid lines in Figure 10a−c, and the dots show a series of comparisons. In the top and bottom plots, comparisons are made to the steady-state expression (eq 3.18b), and the middle panel compares to the much lower density rate constants in the upper panel.

Figures 10a−c demonstrate that the steady-state approximation gives a very accurate rate constant at the equilibrium point.
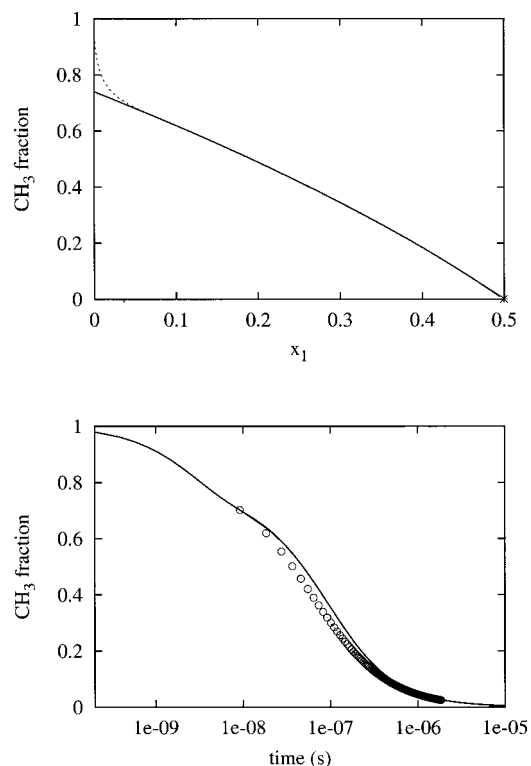
Figure 11. Trajectory for the system in the top panel of Figure 8, but with a pressure of 1000 Torr, shown as a dashed line in the top plot. The slow manifold is shown as a solid curve. The time development of the trajectory is shown in the bottom plot as a solid line, and a trajectory calculated with the phenomenological rate law, as open circles, with the rates calculated at equilibrium (Figure 10c).

It also demonstrates that the density dependence is negligible at equilibrium. However, the rate constant does change away from equilibrium, giving a second type of transient in addition to the one shown in Figure 8. Figures 10d−f show rate constants as functions of y. All parameters are the same as they were in the plots in the left column except for the value of c in the top panel, which has been increased from 3×10^{11} to 1×10^{13}. These plots demonstrate that as density increases there is a change in the rate constant away from equilibrium, something that is not observed in the steady-state approximation. Also included in Figures 10e and f are results from eq 3.19 (shown as dots), demonstrating that this equation is a reasonable correction to the constant rate constant.

Comparisons are made in Figure 7c between trajectories calculated for the Lindemann mechanism and those calculated for the phenomenological rate law with rate constants calculated at equilibrium. The dots are for a simulation starting with pure unexcited ethane ($x_1 = 0.5$), and the open circles are for pure excited ethane ($x_2 = 0.5$). The first initial condition places the trajectory on the 1-D manifold, and the rate constant for this set of parameters does not vary with methyl fraction (Figure 10d), thus making the rate law essentially exact. However, if an initial condition is started off the manifold, the phenomenological rate law is not accurate until the trajectory has reached the manifold, as demonstrated with the open circles.

Figure 10f shows that even when the motion lies on a 1-D manifold it is possible for the time dependence of the species to be different than the phenomenological rate law. Figure 11 shows a trajectory for this system. The top panel shows the trajectory in the phase plane (dashed line) as it approaches the 1-D manifold (solid line). In the bottom panel, the solid line shows the time dependence of the trajectory and the open circles

Association/Dissociation Kinetics

J. Phys. Chem. A, Vol. 106, No. 24, 2002 **5869**

show a trajectory modeled by the rate law. This plot demonstrates that even after the trajectory reaches the manifold its time-dependent behavior is not accurately modeled by the phenomenological rate law.

F. Summary. This section has shown that a geometric investigation of the Lindemann mechanism provides a detailed understanding of the global dynamics, including asymptotic and transient behavior. For example, it provides a means of partitioning the trajectories into dissociative and associative, thus quantifying intuition concerning vibrational relaxation versus dissociation or association as pressure changes. This task is accomplished with the fast manifold. Whereas the slow manifold is accurately modeled by the steady-state approximation under most circumstances, there does not appear to be an analogous way to generate the fast manifold other than with the present approach.

This section has highlighted some of the dynamics for the Lindemann mechanism with association using examples chosen to preview the master equation studied in the rest of the paper. The methods presented here were used to study the master equation with association, particularly those methods used to calculate association rate constants. In particular, it will be shown how the method of extracting rate constants described in section IIIE gives flexibility in avoiding numerical errors associated with small eigenvalues of matrices.

IV. Master Equation

It is well known that the Lindemann mechanism is not a complete picture of the pressure dependence of unimolecular reactions,[38] so the geometric analysis of the previous two sections is extended to the master equation, which is more accurate. Although it is difficult to picture some of the results shown in the previous two sections for the master equation, because of its higher dimensionality, it is possible to implement many of the methods presented in sections II and III. Others, such as the basins described in Figure 5, still provide a means of thinking about the phase space structure of the full master equation, which is similar to that of the Lindemann mechanism. Specifically, in this section, we will discuss the methyl recombination reaction whose pressure dependence has been the subject of many experimental[39−47] and theoretical studies.[3,17,48−50]

A. Rate Equations and Constants of the Motion. A master equation for the processes pictured in eq 2.2 can be written as[2,3]

$$\frac{d\rho_i^{C_2H_6}}{dt} = \omega \sum_{j=1}^m P_{ij}\rho_j(t) - \omega\rho_i^{C_2H_6}(t) - k_i\rho_i^{C_2H_6} + R_i(t) \quad (4.1)$$

$$\frac{d\rho^{CH_3}}{dt} = 2\sum_{i=1}^m k_i\rho_i^{C_2H_6} - 2\sum_{i=1}^m R_i \quad (4.2)$$

where, to be consistent with ref 51, densities are used instead of concentrations. These equations describe the discrete form of the integro-differential master equation.[1,2] The subscripts in eqs 4.1 and 4.2 refer to the ro-vibrational levels of ethane in terms of a set of m bins. There can be transitions between the bins, whose rates are described by the products of the transition moments P_{ij} and the collision frequency ω. The buffer gas that collides with ethane is argon. There are bins whose energies are above the dissociation energy, and these can lead to formation of two methyl radicals with the rate constant k_i. There is also a term $R_i(t)$ that describes the formation of an ethane molecule in bin i from two methyl radicals, which will be explicitly shown below. For bins below the dissociation energy,

k_i and R_i are zero. The P_{ij} values are calculated via the exponential gap model.[1,2] A useful characterization of the strength of this transition moment is the average energy transferred per downward transition,[1,2] which is labeled ΔE_d in the remainder of the paper.

Because the P_{ij} values are subject to microscopic reversibility,[1,2] the expressions in eqs 4.1 and 4.2 can be summed to reveal a constant of the motion that is similar to that in eq 2.4

$$c_\rho = 2\sum \rho_i + \rho_d \quad (4.3)$$

where the superscripts have been dropped and ρ_d refers to the density of the methyl radicals. After collecting terms in eqs 4.1 and 4.2 and dividing by c_ρ, these equations can be rewritten as

$$\frac{dg_i}{dt} = \sum_j R_{ij}g_j - k_ig_i + k_a^\infty c_\rho\phi_i g_d^2 \quad (4.4)$$

$$\frac{dg_d}{dt} = 2\sum_i k_ig_i - 2k_a^\infty c_\rho g_d^2 \quad (4.5)$$

with k_a^∞ referring to the infinite pressure limit of the association rate constant and the term $R_i(t)$ now defined with

$$\phi_i = \frac{k_if_i}{\sum_i k_if_i} \quad (4.6)$$

with f_i referring to a Boltzmann population in bin i.[52] The g's are defined as

$$g_i = \frac{\rho_i}{c_\rho} \quad (4.7a)$$

$$g_d = \frac{\rho_d}{c_\rho} \quad (4.7b)$$

and

$$2\sum_i g_i + g_d = 1 \quad (4.8)$$

For bins below the dissociation energy, $\phi_i = 0$ because $k_i = 0$.

In all calculations reported here, the master equation is divided into 531 bins of 100 cm^{-1} each. Because the dissociation energy for ethane from ref 17 is 30 613 cm^{-1}, the last 225 bins are above the dissociation energy. The total population in these bins is defined as

$$g^* = \sum_{E_i > E_d} g_i \quad (4.9)$$

Although it is straightforward to integrate all components of eqs 4.4 and 4.5, the very slightly reduced system of eq 4.4 is actually integrated with g_d calculated from eq 4.8. It will also be necessary to examine the Jacobian matrix for eq 4.4 under this constraint. The elements of the Jacobian are

$$J_{ij} = \frac{\partial F_i}{\partial g_j} = R_{ij} - 4k_a^\infty c_\rho\phi_i g_d \quad (4.10)$$

where F refers to the right-hand side of eq 4.4. Equation 4.4 demonstrates that for bins above the dissociation energy, where

ϕ_i is nonzero, there is a dependence on g_d that is consistent with that in eq 3.5.

B. Global Dynamics. The global dynamics of the master equation is similar to that of the Lindemann mechanism in section III, and the treatment here follows that of section IIIA without the explicit calculation of basin boundaries that are difficult to define because of the high dimensionality of the system.

1. Fixed Points. There are two fixed points away from infinity, as there were in the phenomenological rate law of section II and the Lindemann mechanism of section III. By defining the reduced Boltzmann distribution values for the bin populations as

$$g_i = \gamma f_i \qquad (4.11)$$

and substituting into eq 4.4, it follows that

$$\frac{\mathrm{d}g_i}{\mathrm{d}t} = 0 \ \text{ for } \ E_i < E_d \qquad (4.12)$$

because there is microscopic reversibility of the R_{ij} parameters in eq 4.4. For bins whose energies are above the dissociation energy,

$$\frac{\mathrm{d}g_i}{\mathrm{d}t} = -\gamma k_i f_i + k_a^\infty c_\rho \phi_i g_d^2 \qquad (4.13)$$

By setting the left sides equal to zero in eq 4.13 and summing over i, the following is obtained:

$$0 = -\gamma K_{eq} + c_\rho(1 - 2\gamma)^2 \qquad (4.14)$$

This expression results from eqs 4.6 and 4.8 and the definition of k_d^∞. The standard result for the value of the methyl radical at the fixed points (e.g., eq 3.11b) is obtained:

$$g_d = \frac{1}{c_\rho}\left(\frac{-K_{eq}}{4} \pm \sqrt{\frac{K_{eq}^2}{16} + \frac{c_\rho K_{eq}}{2}}\right) \qquad (4.15)$$

Once again, the minus sign in eq 4.15 refers to a saddle point, and the plus sign, to the equilibrium point; the saddle point lies on the ethane-rich side of equilibrium. In all our calculations, the saddle point has one positive real eigenvalue and 530 eigenvalues that have negative real parts.

The positions of the equilibrium and saddle points are shown as a function of temperature for two different values of c_ρ in Figure 12. Because the equilibrium constant favors ethane formation at lower temperature, the saddle and equilibrium points lie very close together there. At higher temperature, the thermodynamics favors dissociation of ethane to methyl radicals, and the saddle and equilibrium points then lie far apart.

Although it is difficult to picture the multidimensional phase space out to infinity, as was done in Figures 4 and 9, fixed points at infinity can be found using the procedure described in chapter 3 of ref 35. In the coordinate system of eq 3.13, the saddle point at infinity is

$$u_i = 0, \qquad\qquad E_i < E_{diss} \qquad (4.16a)$$

$$u_i = \frac{-\phi_i}{\sqrt{1 + \sum_j \phi_j^2}}, \qquad E_i > E_{diss} \qquad (4.16b)$$

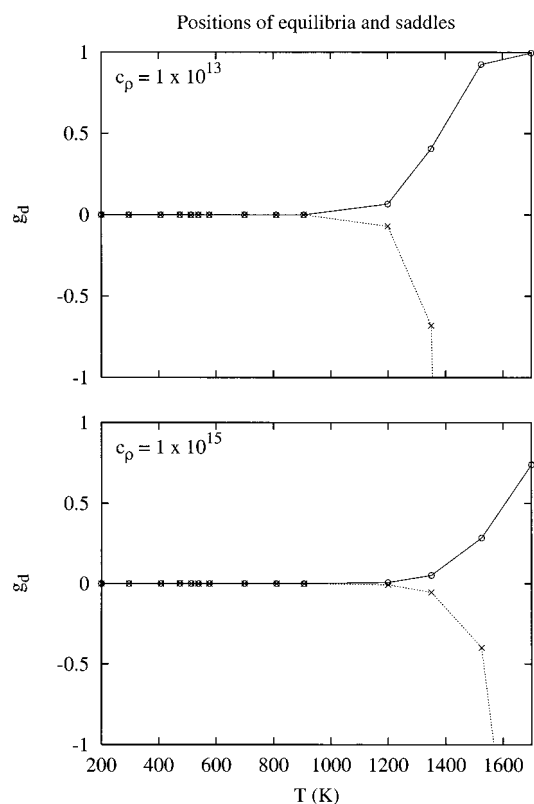Positions of equilibria and saddles

Figure 12. Positions of the equilibrium and saddle points for the master equation shown at a range of temperatures for two values of c_ρ (eq 4.3). The open circles show the equilibrium points, and the $\times$'s show the saddle points, which are in the nonphysical region of phase space ($g_d < 0$).

with ϕ_i defined in eq 4.6. In all the cases studied here, this saddle point lies in the basin of the equilibrium point.

2. Low-Dimensional Manifolds. The final approach to equilibrium for the master equation is a 1-D manifold, as it was in section III for the Lindemann mechanism. The 1-D manifold is the nonlinear analogue[20] of the eigenvector whose eigenvalue is used to generate rate constants for the linear master equation.[1,2] Because there are once again two approaches to equilibrium, the 1-D manifolds are generated in two pieces. The ethane-rich side of the manifold is generated with the saddle-point method of ref 19 using the saddle points pictured in Figure 12. The dynamics associated with these saddle points was referred to as "idealized manifold dynamics" in ref 19. The methyl-rich side of the manifold is generated from the saddle point at infinity that is described in eq 4.16. Figure 13 shows the results of these procedures and compares the methyl-rich portion of the manifold to the predictor–corrector method of ref 19. Because the two methods give essentially the same result, this portion of the manifold is generated from the saddle point at infinity in the rest of the paper.

Figure 14 illustrates the dynamics associated with the 1-D manifold. The top panel shows the (g_d, g_1) plane and the bottom, the (g_d, g^*) plane. The 1-D manifold is shown as a thick solid line, and several trajectories are shown as dashed lines. The equilibrium point [$(g_d, g_1, g^*) = (0.405, 4.46 \times 10^{-5}, 1.20 \times 10^{-6})$] is shown as a large open circle in both panels. Figure 14 demonstrates that all trajectories merge with the manifold on their way to equilibrium. The bottom panel of Figure 14 shows that the 1-D manifold is nonlinear, although it is close to linear for the projection shown in the top panel.

The behavior of two of the trajectories is illustrated by four sets of symbols. One of these trajectories was started at (g_d, g_1,

Association/Dissociation Kinetics

J. Phys. Chem. A, Vol. 106, No. 24, 2002 **5871**

T = 1350 K, $\Delta E_d = 200$ cm^{-1}, P = 1000 torr, $c_\rho = 1 \times 10^{13}$
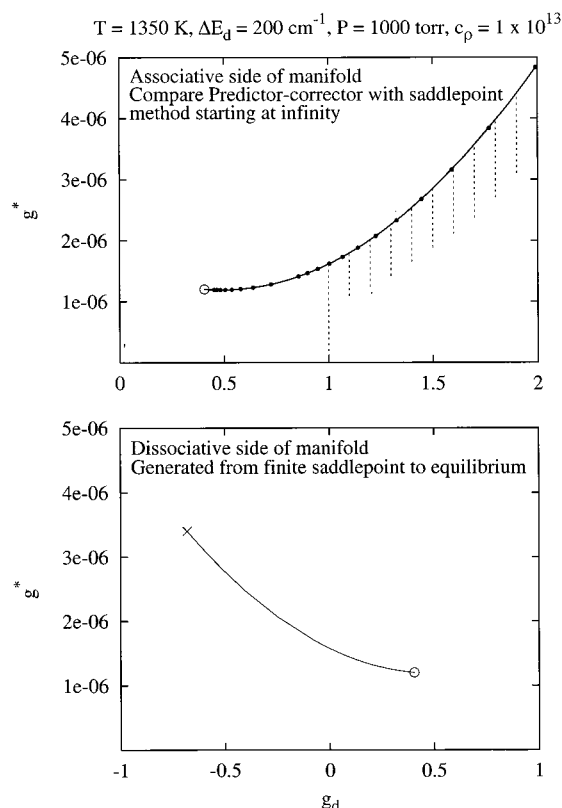
Figure 13. One-dimensional manifolds have two pieces, one on the methyl-rich side of equilibrium (top panel) and the other, the ethane-rich end. The top panel shows the generation of the manifold with two methods, the saddle point and the predictor−corrector methods (dashed lines), which agree. The saddle point is at ∞, which demonstrates that the point gives accurate manifolds, and is used throughout the rest of the paper. The bottom panel generates the manifold from the finite saddle point, the ones shown with ×'s in Figure 12.

g^*) = (0.6, 0.2, 0.0) and the other, at $(g_d, g_1, g^*) = (0.4, 0.0, 0.3)$ with $g_{350} = 0.3$. Symbols describe the following time ranges: solid dots, 50 → 120 ns; ×'s, 0.21 → 0.91 μs; open circles, 3.1 → 8.1 ms; triangles, 0.011 → 0.091 s. The second trajectory has the same order of symbols, but the time ranges are 1 → 12 ns; 22 → 92 ns; 0.11 → 1.1 μs; and 1 → 5 ms. Figure 14 shows that the open circles and the triangles lie on the manifold for the first trajectory and the triangles lie on the manifold for the second trajectory. These symbols indicate that trajectories typically take ∼1 μs to reach the manifold and tens of milliseconds to get within a few percent of equilibrium for $c_\rho = 1 \times 10^{13}$ molecules/cm^3.

More information can be gleaned about the dynamics for the two trajectories. The total fraction for the bins below dissociation is $1 - g_d - g^*$. Thus, the symbols indicate that the first trajectory that starts at $g_d = 0.6$ and $g_1 = 0.2$ initially relaxes with little dissociation (solid dots and ×'s) over the course of ∼1 μs and reaches the manifold. Along the manifold (open circles and triangles), the populations in the bins above dissociation remain nearly constant as the system approaches equilibrium, whereas there is considerable recombination, with g_d decreasing from 0.6 to 0.4. Because g^* remains nearly constant, it can be inferred that the g values for the bins below dissociation increase by 0.1, with the fraction in the ground-state bin shown on the top panel. All trajectories that reach the manifold on the methyl-rich side of equilibrium exhibit this behavior.

Trajectory 2 in Figure 14 that started at $g_d = 0.4$ and $g^* = 0.3$ exhibits the following behavior. Over the first 12 ns (solid
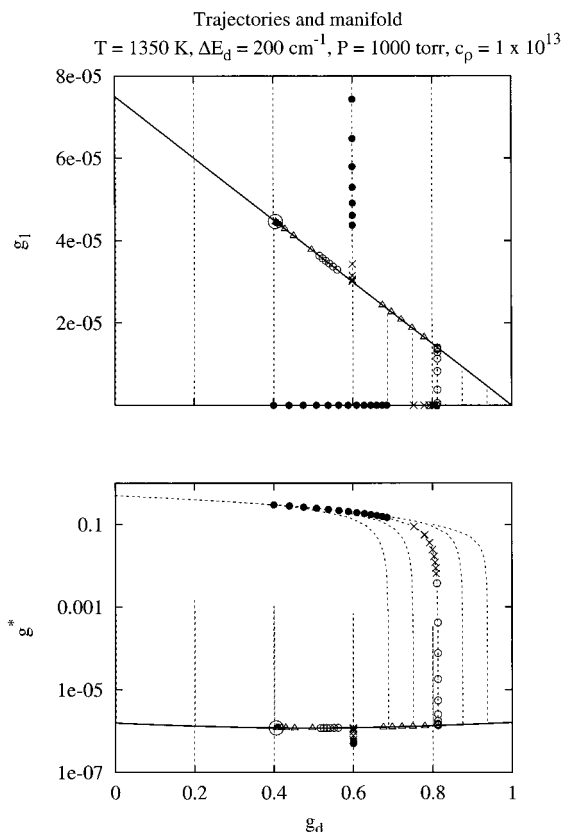

Trajectories and manifold
T = 1350 K, $\Delta E_d = 200$ cm^{-1}, P = 1000 torr, $c_\rho = 1 \times 10^{13}$

Figure 14. Set of trajectories (dashed lines) shown for the master equation, at the values of the parameters in the title of the plot. Two projections are shown, with g^* defined in eq 4.9. The 1-D manifold is plotted as a solid line, and the plots demonstrate that trajectories merge with the manifold. Portions of two trajectories are shown as a set of symbols. The first starts at $(g_d, g_1, g^*) = (0.6, 0.2, 0.0)$, and the second, at (0.4, 0.0, 0.3). The four time ranges for trajectory 1 are ●, 50 → 120 ns; ×, 0.21 → 0.91 μs; ○, 3.1 → 8.1 ms; △, 0.011 → 0.091 s. The four time ranges for trajectory 2 are: ●, 1 → 12 ns; ×, 22 → 92 ns; ○, 0.11 → 1.1 μs; △, 1 → 5 ms.

dots), there is almost exclusive dissociation of ethane into methyl. The ×'s and open circles indicate that from 0.3 to 1.1 μs there is considerable relaxation from the excited-state bins into those below dissociation, with little additional dissociation. After the trajectory reaches the 1-D manifold, it exhibits the same behavior as the first trajectory, although the final approach to equilibrium is not shown.

The symbols in Figure 14 demonstrate that there are stages to the process, indicating a dimensional cascade as suggested in ref 23: before the phase space of the master equation shrinks to the 1-D manifold and eventually to the zero-dimensional equilibrium point, it may shrink through a series of higher-dimensional manifolds.

3. Investigation of Transient Behavior for the Experimental Initial Conditions. Although Figure 14 exhibited interesting transient behavior on the way to the 1-D manifold, the experimental initial condition $g_d = 1$ exhibited none because it lies directly on the 1-D manifold. However, because relaxation occurs in a series of steps, transients for this initial condition often occur, unlike that for the Lindemann mechanism, where relaxation is a single-step process. Such transient behavior is most common for the master equation at high density and relatively small values of ΔE_d.

Figure 15 shows two of these cases, with the top two panels showing projections of the phase space onto the g_d/g_1 plane and the bottom two panels showing the time development. The
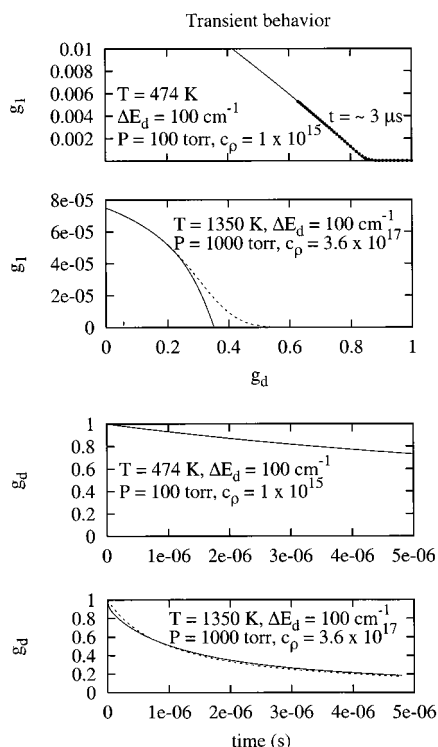
Figure 15. Transient behavior demonstrated for the experimental initial condition $g_d = 1.0$ (pure methyl) because the 1-D manifold does not cross the g_d axis at (1.0, 0.0) in the top two panels. The top panel shows the case at $T = 474$ K, and the second, $T = 1350$ K, with the trajectories started at the experimental initial conditions shown as a set of dots in the top panel and a dashed line in the second panel. The trajectory in the top panel still follows the phenomenological rate as demonstrated in the third panel, but the trajectory at $T = 1350$ K does not (fourth panel, compare the dashed line with the solid line). The text has further details.

phase-space pictures demonstrate that the experimental initial conditions lie away from the manifold, with the trajectory on the top panel taking ~3 μs to reach the manifold. The bottom two panels show the time development of the experimental initial conditions and compares them to the phenomenological rate law with the constants calculated in section IVC (dashed lines). These panels demonstrate that transients in phase space may (bottom panel) or may not (third panel) indicate the breakdown of the phenomenological rate law.

4. Dynamics on the Manifold. Because the 1-D manifolds of section IVB.1 describe the asymptotic motion and are analogous to the eigenvectors for the linear master equation,[20] they provide the means to test the approximations that were used to calculate association rate constants in ref 17. These approximations were developed in ref 3, are implemented in the program Variflex,[18] and rely on several important assumptions. The first assumption is that there is a state ("cemetery state") in ethane that divides the relaxation in the following way: there are transitions from states above the cemetery state to those below it, but there are no transitions in the opposite direction. It is further assumed that all bins below the cemetery state have a Boltzmann distribution relative to each other, with the temperature of the distribution being the bath temperature. The final assumption is that the bins above the cemetery state are in the steady state, meaning that the derivatives on the left-hand side of eq 4.4 are zero.

Figure 16 follows the vibrational distribution (dashed lines) along the manifold and is typical for the cases studied here. Figure 16 investigates the same system as do Figures 13 and 14, which has its equilibrium point at $g_d = 0.405$. The top six

panels are on the ethane-rich side of equilibrium, and the bottom six are on the methyl-rich side. The manifold is followed as a function of g_d, which is labeled on each plot. The vibrational distribution is compared to a Boltzmann distribution, plotted as a solid line. The probabilities in the Boltzmann distribution sum to $1 - g_d$, which is the fraction of ethane present.

Figure 16 demonstrates that as equilibrium is approached the vibrational distribution becomes closer to a Boltzmann distribution. It also shows that the lower-energy bins are much closer to equilibrium than are the higher-energy bins, whose populations increasingly deviate from a Boltzmann distribution. On the ethane-rich side of equilibrium, the deviation is on the low side of the Boltzmann distribution, and on the methyl-rich end, it is higher than the Boltzmann distribution. Because the sum of the probabilities is $1 - g_d$, deviations in the higher-energy bins are compensated for by deviations in the lower-energy bins that are similar in magnitude but are much smaller relative to the values of g_i for the bins.

Figure 17 tests the steady-state assumption for the system of Figures 13, 14, and 16, and Figure 18 tests it for one of the systems in Figure 15, which showed transient behavior in the top panel of that Figure. Both plots indicate that the steady-state approximation gets better as equilibrium is approached at $g_d = 0.405$ in Figure 17 and $g_d \approx 0.0$ in Figure 18. In Figure 17, dg_i/dt is small for many bins below dissociation at bin 307 but has noticeably smaller values at and above dissociation. In Figure 18, the values are never small away from equilibrium until the dissociation threshold is reached, and then there is a sharp drop. Because of the relative magnitude of dg_i/dt in Figure 17, the steady-state approximation is probably valid well below the dissociation threshold for that case away from equilibrium, but for the case in Figure 18, the approximation is not valid below the threshold, except close to equilibrium.

The case shown in the second and fourth panels of Figure 15 showed significant transient effects. Figure 19 examines the vibrational distribution for this case. All panels examine the methyl-rich end of the manifold, with equilibrium at $g_d \cong 0$. The first and third rows repeat the analysis of Figure 16, and the second and fourth rows, the analysis of Figures 17 and 18. These analyses demonstrate that even the lowest bins are significantly different than a Boltzmann distribution away from equilibrium ($g_d = 0.336$) and that the steady-state approximation is poor even at $g_d = 0.036$ as the manifold approaches equilibrium. The system studied in Figure 19 will be revisited below in Figure 21, where it will be shown that the local rate constant changes with g_d and is consistent with the breakdown of the methods in ref 17.

C. Rate Constants. Rate constants can be estimated in the same manner as they were in section IIIE using the Jacobian matrix whose elements were shown in eq 4.10. Because the Jacobian depends on the density of the methyl radicals, it will not be constant, although it will be shown below for dilute cases, which are typical of experiments for methyl recombination,[39−47] that the rate constants are constant over the whole domain, which is something that could be observed analytically in section IIIE for the Lindemann mechanism. It will be shown in this subsection how to generate the rate constant for a wide range of temperatures and pressures, as reported in ref 17, in a manner that does not require the approximations used there. For nondilute cases, rate constants are dependent on g_d for a given c_ρ, and there is also a dependence of the rate constants on c_ρ, as discussed below.

1. Trends in Rate Constants. By analogy to eq 3.18, the rate constants are calculated from the largest eigenvalue of the

Association/Dissociation Kinetics

J. Phys. Chem. A, Vol. 106, No. 24, 2002 **5873**

Distributions along manifold vs. Boltzmann, T = 1350, ΔE_d = 200 cm^{-1}, P = 1000 torr, ρ = 1 x 10^{13}
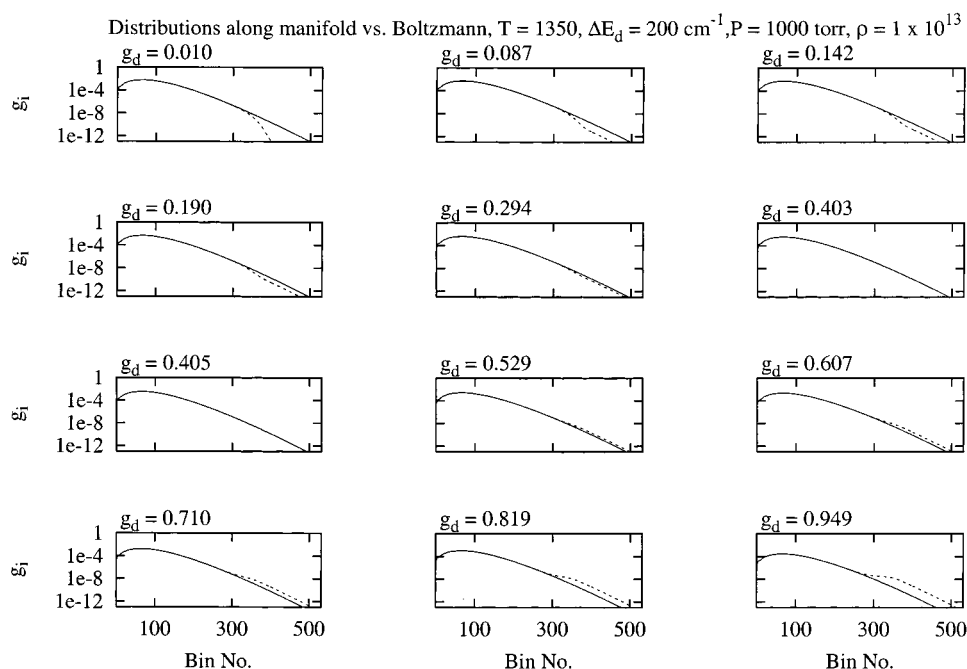

Figure 16. Vibrational distribution along the manifold, parametrized by the values of g_d, which are shown on each panel. The solid lines in the panels show the Boltzmann distribution, and the dashed lines show the actual vibrational distributions. Equilibrium is at $g_d = 0.405$; the top six panels are on the ethane-rich side of equililbrium, and the bottom six panels, on the methyl-rich side. These panels demonstrate that as the system approaches equilibrium along the 1-D manifold it becomes more Boltzmann-like. On the ethane-rich side, the populations of high-energy bins are smaller than Boltzmann populations, and on the methyl-rich side, they are larger.
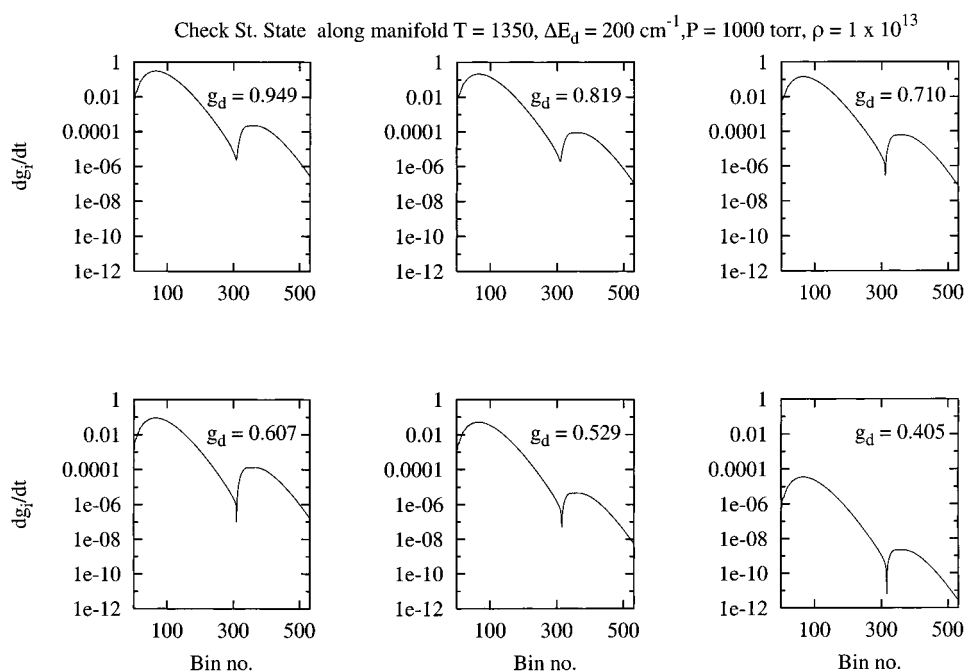
Check St. State along manifold T = 1350, ΔE_d = 200 cm^{-1}, P = 1000 torr, ρ = 1 x 10^{13}

Figure 17. Test of the steady-state approximation. The value of the time derivative on the left-hand side of eq 4.4 is plotted for the vibrational distribution along the low-dimensional manifold parametrized by the value of g_d.

Jacobian matrix, whose elements are shown in eq 4.10 (because the matrix is calculated with the constraint of eq 4.8, all of the eigenvalues are negative and the largest eigenvalue is the "least negative"). In the notation of this section, the rate constant is written as[53,54]

$$k_a = \frac{-\lambda_1}{K_{eq} + 4c_\rho g_d} \qquad (4.17)$$

Once again, the rate constant is a function of the methyl fraction. For low c_ρ, this does not pose a problem for the Lindemann

mechanism for the reasons discussed in section IIIE. Figure 20 shows the results for a dilute case of 10 ppm at 1000 Torr, which has a slightly higher density than that of Figure 14. The top panel shows the largest eigenvalue as a function of the methyl fraction, g_d, and the bottom two panels show the next largest eigenvalue and the lowest eigenvalue, respectively. These demonstrate that the only eigenvalue that changes appreciably with the methyl fraction is the largest one, which increases approximately linearly. Because the second term in the denominator of eq 4.17 is much larger than the first, there is essentially
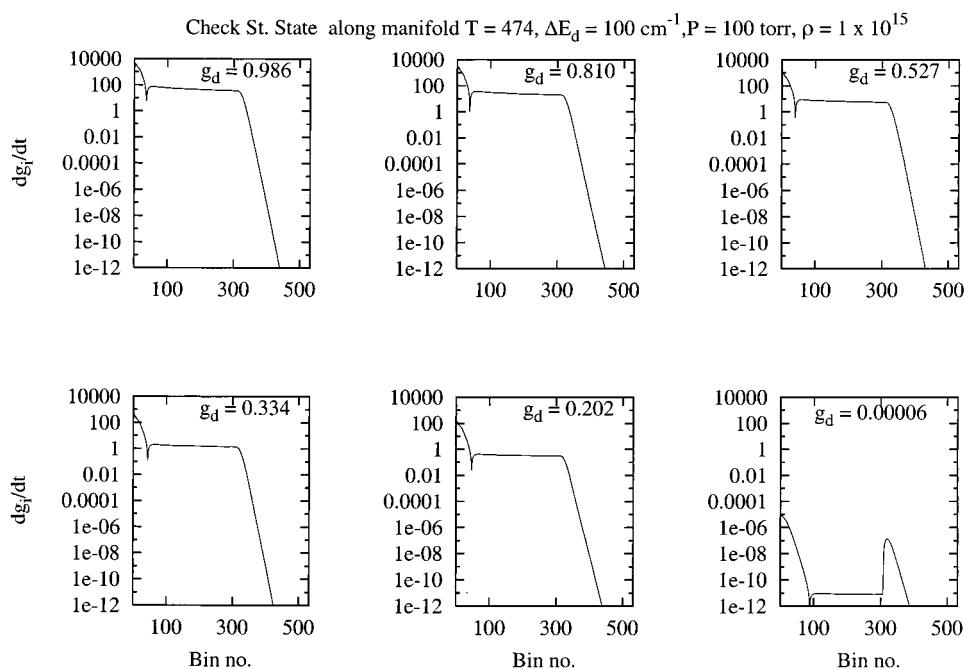
Check St. State along manifold T = 474, $\Delta E_d = 100 \text{ cm}^{-1}$, P = 100 torr, $\rho = 1 \times 10^{15}$

Figure 18. These panels give the same information as does Figure 17 but for a different set of master equation conditions.
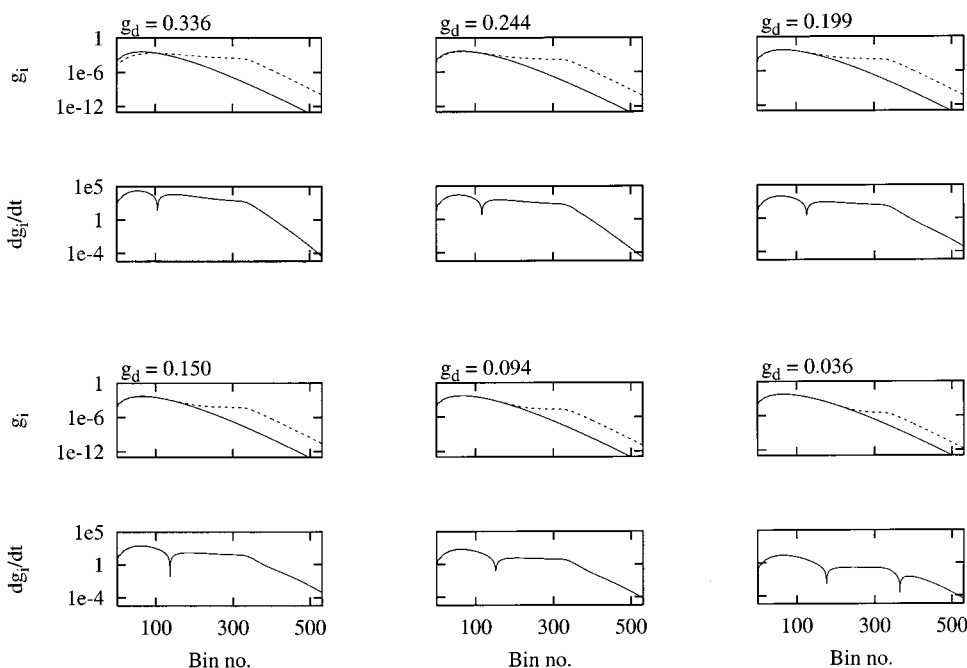
Figure 19. The case in the second and fourth panels of Figure 15 is studied using the same measures as in Figures 16−18. These plots demonstrate that this case is much further from a Boltzmann distribution than the one in Figure 16 and is considerably further from the steady state than are those in Figures 17 and 18.

a linear dependence of the denominator with respect to the methyl fraction. Because Figure 20 shows that λ_1 also has a linear dependence, the linear dependence of the denominator is canceled by the linear dependence of the numerator in eq 4.17, and the third panel in the left column of Figure 21 demonstrates that the rate constant is constant across the entire phase space. The other panels in the left column of Figure 21 show that the rate constants are also constant across the full phase space for other values of ΔE_d.

The situation is different for less dilute cases. The right column of Figure 21 shows a case where dilution is 5%. The second panel of this column shows the same case as shown in the second and fourth panels of Figure 15. The plots in the right

column of Figure 21 demonstrate that the rate constant need not be constant when the density of the reactive species is not very high. Comparison of the third panel in the right column and the second panel of Figure 15 demonstrates that even after the trajectory has reached the 1-D manifold the rate constant is not constant. This result is interesting because after the system has reached the 1-D manifold it should be described by a 1-D rate law. This idea will be further explored in section V.

2. Rate Constants Near Equilibrium. A natural way to address the problem of changing rate constants is to calculate them at or near equilibrium. The top three panels of Figure 22 outline this procedure for the case in the third panel of the right column of Figure 21 but at several different values of c_ρ, which
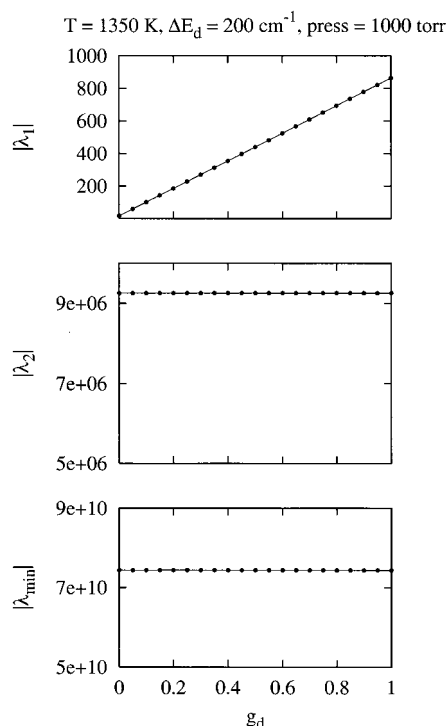
Figure 20. Eigenvalues of the Jacobian of eq 4.10 shown as a function of g_d. The top panel shows the largest eigenvalue, the second panel, the next largest, and the bottom panel, the smallest. The largest eigenvalue varies approximately linearly with g_d, and the others are nearly constant.
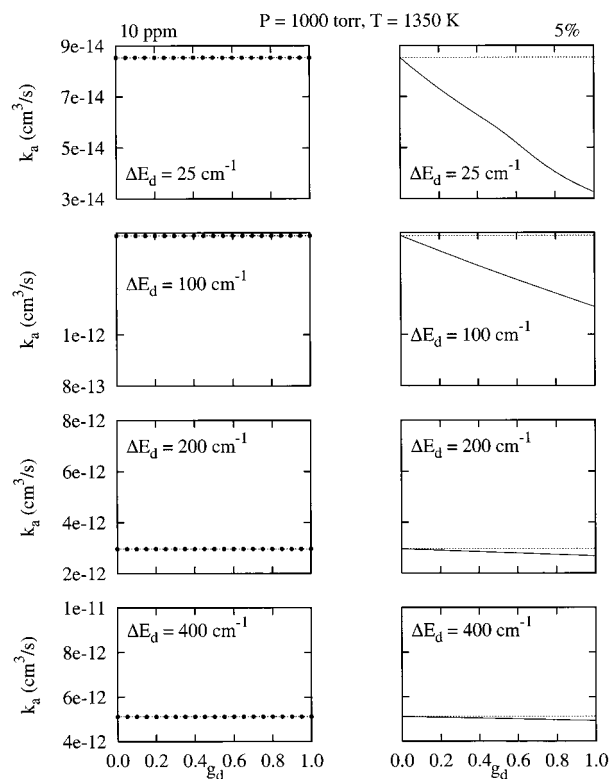

Figure 21. Association rate constants calculated using two different values of c_ρ (eq 4.17) and plotted as functions of g_d. The left column repeats the case in Figure 20, and the right column shows a much less dilute case at the same pressure. Although the left column shows that the association rate constant is in fact constant, the right column shows otherwise.

is 3.6×10^{17} molecules/cm^3 in Figure 21. These panels show that λ_1 (top panel) and g_d at equilibrium (second) change in
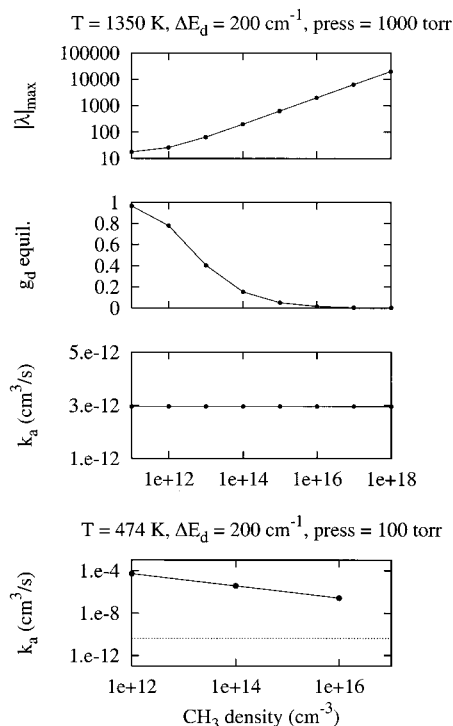

Figure 22. The top three panels demonstrate that rate constants can be extracted at equilibrium by diagonalizing the matrix in eq 4.17. The top panel shows the largest eigenvalue, the second panel, the equilibrium values of g_d, and the third panel, k_a as a function of c_ρ. These demonstrate that the rate constant is constant over a large range of density when calculated in this manner. However, this result cannot always be attained because of numerical error, as demonstrated in the bottom panel, where k_a is not constant and is considerably in error when compared to the correct value shown as a dotted line.

such a manner as to leave eq 4.17 constant. However, the situation in the top three panels of Figure 22 is not always realized. The bottom panel of Figure 22 shows the case for $T = 474$ K where k_a is far from constant as a function of methyl density and also far from the actual rate constant that is shown as a dotted line. The reason this case fails is that λ_1 is so small that the diagonalization routine is unable to accurately calculate it, and more sophisticated procedures need to be employed.[55,56] Equation 4.17 would give accurate answers if λ_1 were correctly calculated because g_d is very small and would compensate for it.

The problem of small eigenvalues plagues the calculation of association rates. A natural procedure for calculating them would be to calculate the dissociation rate constant, which is straightforward depending on the diagonalization of the matrix,[1,2] but as is the case with the system studied here, the dissociation rate constant is so small at $T = 474$ K that it is difficult to extract, and other procedures are used that involve approximations[3] or more sophisticated techniques are used to extract the largest eigenvalue for the dissociation rate constant.[55,56]

3. Beating the Small Eigenvalue Problem. The top panels of Figures 20 and 22 demonstrate that the largest eigenvalue of the matrix of eq 4.10 changes with the density constant c_ρ, and we employ this change to beat the small eigenvalue problem. First, eq 4.17 is rewritten as

$$c_\rho = \frac{-(\lambda_1^0 + k_a K_{eq})}{4 k_a g_d^0} \qquad (4.18)$$

where g_d is fixed in eq 4.18 at g_d^0, which here is taken to be 0.05, and λ_1 is fixed at λ_1^0, here taken to be -0.1. The

T = 1350 K, ΔE_d = 200 cm^{-1}, Aim for λ_{max} = -0.1 at g_d = 0.05
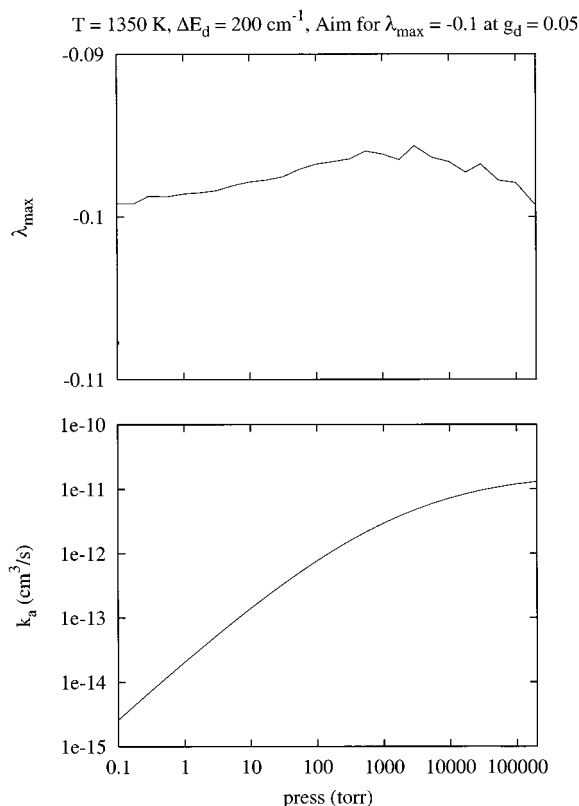

Figure 23. By using the prescription outlined in the text, c_ρ can be adjusted so that the maximum eigenvalue falls near −0.1, as demonstrated in the top panel. These eigenvalues lead to the calculated k_a-values that are shown in the bottom panel.

magnitude of λ_1 is sufficiently large that the numerical problem encountered in the bottom panel of Figure 22 is avoided. The value of g_d is acceptable because it is near equilibrium at high density, where difficulties arise (e.g., the right column of Figure 21). Although it is far from equilibrium at low density, there are no problems there.

The high-pressure limit of eq 4.18 is

$$c_\rho^\infty = \frac{-(\lambda_1^0 + k_d^\infty)}{4k_a^\infty g_d^0} \qquad (4.19)$$

All quantities are known, and c_ρ^∞ can be calculated for fixed values of λ_1 and g_d. Estimates of k_a at high pressure can be made from eq 4.19. A few calculations at a series of high pressures allow k_a to be extrapolated in eq 4.18 to lower pressures, and values of c_ρ can be chosen to permit λ_1 to be approximately −0.1 when diagonalizing the Jacobian matrix of eq 4.10. The actual value of λ_1 from the diagonalization is always substituted into eq 4.17 to obtain the true value of k_a. This procedure is continued to lower pressure, with the last several values of k_a that are calculated in the current pressure range used to extrapolate to lower pressure to ensure that λ_1 is near −0.1. The success of this procedure is outlined in Figure 23. The top panel shows that the extrapolation procedure leads to a series of diagonalizations with λ_1 near −0.1. The bottom panel then shows a series of rate constants calculated from λ_1 and eq 4.17.

This procedure allows the calculation of k_a over a large pressure and temperature range using matrix diagonalization, as demonstrated in Figure 24. The rate constants are calculated

at five values of E_d. From bottom to top in each panel, they are 25, 100, 200, 400, and 800 cm^{-1}. The dots in each plot are values calculated in ref 17, and they demonstrate excellent agreement.

V. Rate Law Along the 1-D Manifold

Although the results in the previous section reproduced those of ref 17, they are somewhat unsatisfactory. The rate constants calculated in Figure 24 are near the equilibrium values because Figure 21 showed that for higher densities (right column) the association rate constant varied with position, something that is not surprising because the definition in eq 4.17 includes g_d and λ_1, which depends on g_d. This section describes a more rigorous method for deriving a rate expression, although the method is perhaps more difficult than those described in section IV and methods used elsewhere.

We demonstrated in section IVB that the dynamics reaches a 1-D manifold rather quickly and then proceeds to equilibrium along the manifold. This result suggests that a 1-D rate law should be sufficient to describe the association/dissociation process along the manifold, and the following are investigated:

$$\frac{d\rho^{CH_3}}{dt} = \sum_{n=1} a_n(\rho^{CH_3} - \rho_{eq}^{CH_3})^n \qquad (5.1a)$$

$$\frac{dg_d}{dt} = \sum_n b_n(g_d - g_d^{eq})^n \qquad (5.1b)$$

$\rho_{eq}^{CH_3}$ refers to the equilibrium methyl density, and g_d^{eq} refers to the scaled version of this quantity (eq 4.7b). The quantity dg_d/dt is calculated along the 1-D manifold using the master equation of section IV and is fit to the right-hand side of eq 5.1b. The b_n values and dg_d/dt depend on c_ρ.

Besides providing a density dependence, eq 5.1 also includes terms that are of a higher order than those of the standard rate law of eq 2.3. However, for the cases studied here, it is necessary to include only linear and quadratic terms as demonstrated in the right column of Figure 25, which shows results at $T = 1350$ K for three values of ΔE_{down} and at several different densities. The left column of Figure 25 presents the methyl-rich ends of the 1-D manifolds, and trajectories flow from right to left as demonstrated in the top panel of Figure 14. The right column of Figure 25 shows a scaled version of the rate from eq 5.1b:

$$r_s = \frac{1}{[c_\rho(g_d - g_d^{eq})]} \frac{dg_d}{dt} \qquad (5.2)$$

r_s is negative, with the absolute value shown in Figure 25. The scaled progress variable is defined as

$$z = \frac{g_d - g_d^{eq}}{g_d^{max} - g_d^{eq}} \qquad (5.3)$$

with g_d^{max} equal to the value of g_d on the manifolds as they cross into the physically allowed regions, as shown on the plots in the left column, ranging from less than 0.2 for $c_\rho = 10^{18}$ in Figure 25a to approximately 1.0 for all of the low c_ρ cases in the left column (manifolds are started in nonphysical regions, as described in section IVB).

The right column of Figure 25 includes r_s as a function of z plotted as a solid line. The dots in the plots show linear least-

Association/Dissociation Kinetics

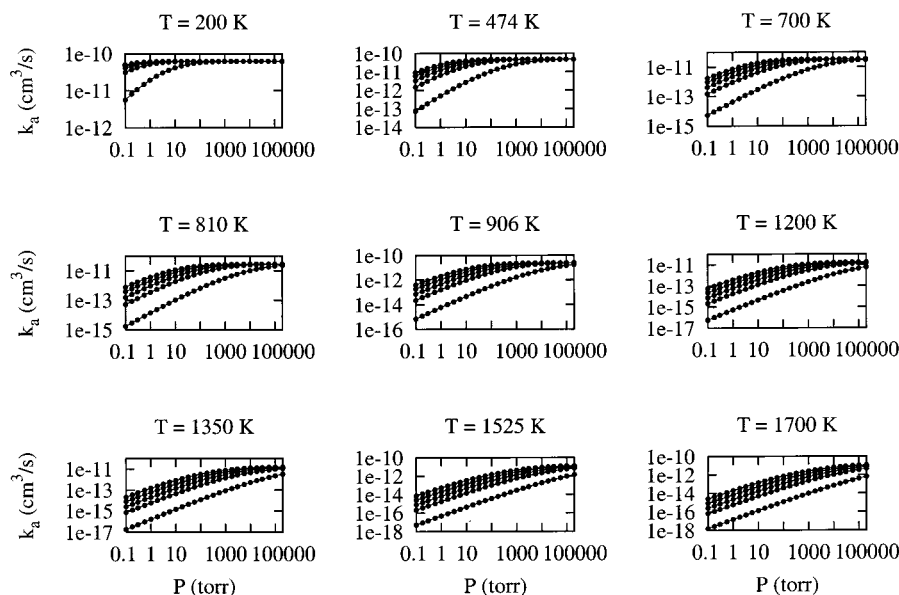*J. Phys. Chem. A, Vol. 106, No. 24, 2002* **5877**

Figure 24. Using the prescription in the text, rate constants can be calculated over a large range of temperature and pressure, as indicated in these plots. The solid dots compare the results here to those calculated in ref 17 and demonstrate that agreement is excellent.

square fits, which are very good, and indicate that only the linear and quadratic terms need be included in eq 5.1b. Under this condition, eq 5.1b can be equated to eq 2.5a to calculate the rate constants for association and dissociation:

$$k_a = \frac{-0.5 b_2}{c_\rho} \tag{5.4a}$$

$$k_d^{(1)} = -b_1 g_d^{eq} + b_2 (g_d^{eq})^2 \tag{5.4b}$$

$$k_d^{(2)} = -b_1 + 2 b_2 g_d^{eq} \tag{5.4c}$$

The b's are the fitting coefficients from eq 5.1b. The superscripts on the left sides of eqs 5.4b and 5.4c indicate that there are two ways to define k_d when making a term-by-term comparison because k_d is the coefficient for both the constant and linear terms in eq 2.5a.

Figure 26 presents the values of k_a, $k_d^{(1)}$, and $k_d^{(2)}$ in (a), (b), and (c), respectively. Included on each panel are points for seven values of c_ρ and four values of ΔE_d. Also included as solid lines are the values of k_a and k_d from ref 17. Figure 26a demonstrates that k_a is nearly constant but is slightly lower at high density and somewhat higher at low density. It would be possible to include this density dependence in eq 5.1b, but that is beyond the scope of this paper.

Although the k_a values in Figure 26 agree with the calculations in section IV and ref 17, difficulties arise for k_d in the bottom two panels and indicate that the rate law of eq 5.1b may be a better representation of the association/dissociation process than is the usual phenomenological rate law of eq 2.5a. However, the expansion coefficients b_1 and b_2 in eq 5.4 have the same sign. Although b_2 remains nearly constant, b_1 changes in a fashion similar to that of g_d^{eq}; the subtraction in eq 5.4 may make the k_d values prone to numerical error, and some caution should be exercised in making conclusions on the basis of changes in k_d values in Figure 26. Nevertheless, the fact that the k_a values are nearly constant in Figure 26 and change in the right column of Figure 21 suggests that the assumption that there is a good equilibrium constant along the full manifold (see eq 4.17) may not be valid.

To probe this idea further, eq 5.4 is rewritten to give

$$\frac{1}{k_a} \frac{k_d^{(1)} - g_d^{eq} k_d^{(2)}}{1 - g_d^{eq}} = \frac{2 c_\rho (g_d^{eq})^2}{1 - g_d^{eq}} \tag{5.5}$$

with b_2 substituted from eq 5.4a. By substituting

$$\frac{2 c_\rho (g_d^{eq})^2}{1 - g_d^{eq}} = \frac{2 c_\rho^2 (g_d^{eq})^2}{c_\rho (1 - g_d^{eq})} = \frac{(\rho_{CH_3}^{eq})^2}{\rho_{C_2H_6}^{eq}} = K_{eq} \tag{5.6}$$

into eq 5.5, the following is obtained:

$$\frac{1}{k_a} \frac{k_d^{(1)} - g_d^{eq} k_d^{(2)}}{1 - g_d^{eq}} = K_{eq} \tag{5.7}$$

which reduces to the standard expression $k_d / k_a = K_{eq}$ only when $k_d^{(1)} = k_d^{(2)}$.

This suggests that there is no well-defined K_{eq} along the full length of the 1-D manifolds for the high-density cases where in Figure 26 $k_d^{(1)} \neq k_d^{(2)}$, although we emphasize again that there is a caveat to this conclusion, as discussed above.

VI. Discussion and Conclusions

A numerical investigation of dissociation/association kinetics has been undertaken in this paper from a geometrical perspective. It was shown how the geometry of phase space varied with temperature, pressure, and density of reactive species for the phenomenological rate law, a Lindemann mechanism, and a master equation describing the recombination of two methyl radicals to form ethane and the dissociation of ethane to form two methyl radicals.

It was shown that a good way of investigating the asymptotic motion of this nonlinear problem was by studying the approach and subsequent motion on a 1-D manifold, which is the nonlinear analogue of the appropriate eigenvector of the linear master equation.[1,2] For the lower-dimensional Lindemann mechanism, the investigation of the 1-D slow manifold was part of a larger analysis of the global phase-space structure of
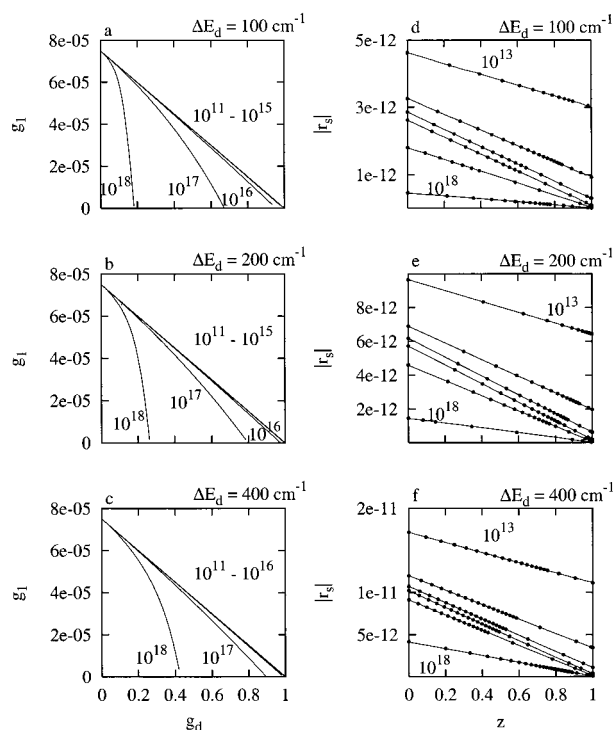
Figure 25. Several 1-D manifolds are shown in the left column at a series of c_ρ values marked on the plots for $T = 1350$ K, $P = 1000$ Torr, and various ΔE_d values labeled on each panel. These demonstrate that as c_ρ gets larger the manifolds become more nonlinear. The right column shows the values of $|r_s|$, defined in eq 5.2, as a function of the progress variable z, defined in eq 5.3. The dots show a fit to the form in eq 5.1b with a maximum n of 2. The dots show that r_s is nearly exactly linear.

the association/dissociation problem, which set the stage for the more realistic and much higher dimensional master equation, where a less thorough mapping of phase space is possible. Although not all of the analysis used for the much lower dimensional problem could be applied to the master equation, it suggested the need for some caution. For example, before using the methods for generating the 1-D manifolds on the methyl-rich side (Figure 13), it had to be established that the saddle point at infinity (eq 4.16 in section IV) was in the basin of attraction of the equilibrium point, something that was discussed in detail for the Lindemann mechanism (section IIIB).

The investigation of the phase-space structure of the Lindemann mechanism and the master equation led to a new method of calculating association rate constants, which was presented in section IVC. It was shown there that association rate constants could be calculated over large temperature and pressure ranges and were in excellent agreement with those calculated previously in ref 17 without using any approximations. However, it was demonstrated that the rate constants varied with position in phase space when the density was high or when ΔE_d was low.

The variation of the rate constant with position is perhaps not surprising, because the master equation is nonlinear, but is nevertheless disconcerting and led to what we view as a more rigorous approach in section V. A new rate law for the association/dissociation process was developed there. It was shown that a quadratic form of eq 5.1b was sufficient to model a set of simulations at $T = 1350$ K and that association rate constants, which varied slightly with density, could be calculated. These results, in conjunction with earlier ones on the change in the local rate constant, suggested that there may be
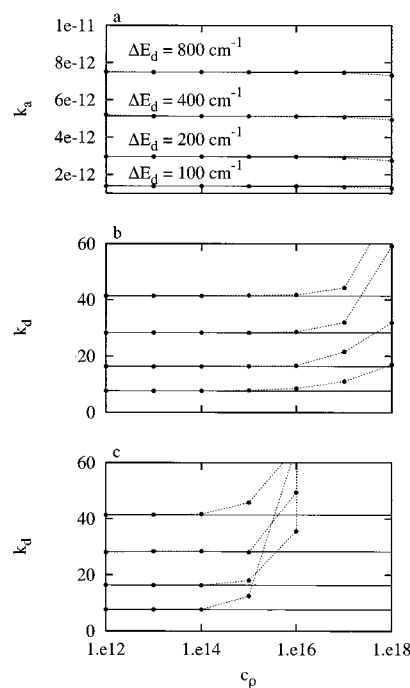

Figure 26. Rate constants can be estimated from the fits in the right column of Figure 25, as described in eqs 5.4a−5.4c. The top plot demonstrates that k_a (dots and dotted line) varies only slightly as a function of c_ρ and compares very favorably with the rate constants calculated in ref 17, shown as the solid lines. The k_d values are much worse, as demonstrated in the bottom two panels. The second panel shows k_d calculated with eq 5.4b, and the bottom panel, k_d calculated with eq 5.4c. The text has further details.

no well-defined equilibrium constant along the length of the 1-D manifold as density increases, although there is one at equilibrium.

Appendix: Generating a Lindemann Mechanism from the Master Equation

The Lindemann mechanism studied in section III laid the groundwork for the methods used for the master equation in section IV, and it was thus desirable to have reasonable parameters for the mechanism. The three parameters for the Lindemann mechanism (eq 3.4) are a, k, and f_1, with f_2 fixed by $f_1 + f_2 = 1$. Parameters were generated by first diagonalizing the Jacobian matrix of eq 4.10 at several values of g_d between 0 and 1 (the minimum and maximum values), and the maximum eigenvalue of the Jacobian of the master equation was fit to a quadratic of the form

$$\lambda_1 = b_0 + b_1 g_d + b_2 g_d^2 \qquad (A.1)$$

The parameters b_1 and b_2 were then equated to the corresponding two terms in the expansion of λ_1 in eq 3.8a, which was generated by expanding the denominator

$$\lambda_1 \cong \frac{-a(4k_a cy + kf_2)}{a + k}\left(1 - \frac{4k_a cy}{a + k}\right) \qquad (A.2)$$

Association/Dissociation Kinetics

J. Phys. Chem. A, Vol. 106, No. 24, 2002 **5879**

giving

$$b_1 = \frac{-4ak_ac}{a+k}\left(1 - \frac{kf_2}{a+k}\right) = \frac{-4ak_ac(a+kf_1)}{(a+k)^2} \cong \frac{-4ak_ac}{(a+k)} \quad \text{(A.3a)}$$

$$b_2 = \frac{a(4k_ac)^2}{(a+k)^2} \quad \text{(A.3b)}$$

Because c is fixed in the simulation and k_a is known, these equations define a and k. The Boltzmann factors are defined from the requirement that the infinite pressure dissociation rate constant must equal kf_2.

The parameters a, k, and f_1 used in most of the calculations were derived from a Jacobian matrix at $T = 1350$, $c_\rho = 1 \times 10^{13}$, $P = 1000$ Torr, and $\Delta E_d = 200$ cm^{-1}. Other parameter sets were generated from this set. Pressure was "adjusted" by scaling a as described in eq 3.14, and c was chosen from the values quoted in the text. The only exceptions to this procedure are for the calculations presented in the bottom panel of Figure 8, where k was scaled by a factor of 0.001 and f_1 and f_2 were chosen to be 0.9 and 0.1, respectively, and for those presented in the bottom panel of Figure 9 whose parameters were calculated from the diagonalization of the Jacobian matrix for the master equation at $T = 474$ K, $c_\rho = 1 \times 10^{18}$, $P = 1000$ Torr, and $\Delta E_d = 100$ cm^{-1}.

References and Notes

(1) Gilbert, R. G.; Smith, S. C. *Theory of Unimolecular and Recombination Reactions*; Blackwell Scientific: Oxford, U.K., 1990.

(2) Holbrook, K. A.; Pilling, M. J.; Robertson, S. H. *Unimolecular Reactions*, 2nd ed.; Wiley: Chichester, U.K., 1996.

(3) Robertson, S. H.; Pilling, M. J.; Baulch, D. L.; Green, N. J. B. *J. Phys. Chem.* **1995**, *99*, 13452.

(4) Barker, J. R. *Chem. Phys.* **1983**, *77*, 301.

(5) Shi, J.; Barker, J. R. *Int. J. Chem. Kinet.* **1990**, *22*, 187.

(6) Bedanov, V. M.; Tsang, W.; Zachariah, M. R. *J. Phys. Chem.* **1995**, *99*, 11452.

(7) Gates, K. E.; Robertson, S. H.; Smith, S. C.; Pilling, M. J.; Beasley, M. S.; Maschhoff, K. J. *J. Phys. Chem. A* **1997**, *101*, 5765.

(8) Vereecken, L.; Huyberechts, G.; Peeters, J. *J. Chem. Phys.* **1997**, *106*, 6564.

(9) Tsang, W.; Bedanov, V.; Zachariah, M. R. *Ber. Bunsen-Ges. Phys. Chem.* **1997**, 491.

(10) Venkatesh, P. K.; Dean, A. N.; Cohen, M. H.; Carr, R. W. *J. Chem. Phys.* **1997**, *107*, 8904.

(11) Frankcombe, T. J.; Smith, S. C.; Gates, K. E.; Robertson, S. H. *Phys. Chem. Chem. Phys.* **2000**, *2*, 793.

(12) Blitz, M. A.; Beasley, M. S.; Pilling, M. J.; Robertson, S. H. *Phys. Chem. Chem. Phys.* **2000**, *2*, 805.

(13) Knyazev, V. D.; Tsang, W *J. Phys. Chem. A* **2000**, *104*, 10747.

(14) Barker, J. R. *Int. J. Chem. Kinet.* **2001**, *33*, 232.

(15) Barker, J. R.; Ortiz, N. F. *Int. J. Chem. Kinet.* **2001**, *33*, 246.

(16) Miller, J. A.; Klippenstein, S. J. *J. Phys. Chem. A* **2001**, *105*, 7254.

(17) Klippenstein, S. J.; Harding, L. B. *J. Phys. Chem. A* **1999**, *103*, 9388.

(18) Klippenstein, S. J.; Wagner, A. F.; Dunbar, R. C.; Wardlaw, D. M.; Robertson, S. H.; *Variflex*, version 1.0; 1999.

(19) Davis, M. J.; Skodje, R. T. *J. Chem. Phys.* **1999**, *111*, 859.

(20) Davis, M. J.; Skodje, R. T. *Z. Phys. Chem.* **2001**, *215*, 233.

(21) Skodje, R. T.; Davis, M. J. *J. Phys. Chem. A* **2001**, *105*, 10356.

(22) Fraser, S. J. *J. Chem. Phys.* **1988**, *88*, 4732.

(23) Roussel, M. R. A Rigorous Approach to Steady-State Kinetics Applied to Simple Enzyme Mechanisms. Ph.D. Thesis, University of Toronto, Toronto, Canada, 1994 and references cited therein.

(24) Roussel, M. R.; Fraser, S. J. *Chaos* **2001**, *11*, 196 and references cited therein.

(25) Maas, U.; Pope, S. B. *Combust. Flame* **1992**, *88*, 239.

(26) Maas, U.; Pope, S. B. *Proc. Combust. Inst.* **1992**, *28*, 103.

(27) Maas, U.; Pope, S. B. *Proc. Combust. Inst.* **1994**, *25*, 1349.

(28) Davis, M. J. *J. Chem. Phys.* **2002**, *116*, 7828.

(29) Brau, C. A. *J. Chem. Phys.* **1967**, *47*, 1153.

(30) Brau, C. A. *J. Chem. Phys.* **1967**, *47*, 3076.

(31) Hogarth, W. L.; McElwain, D. L. S. *J. Chem. Phys.* **1975**, *63*, 2502.

(32) Hogarth, W. L.; McElwain, D. L. S. *Chem. Phys.* **1977**, *19*, 429.

(33) Lim, C.; Truhlar, D. G. *J. Phys. Chem.* **1983**, *87*, 2683.

(34) Benson, S. W. *The Foundations of Chemical Kinetics*; McGraw-Hill: New York, 1960.

(35) Perko, L. *Differential Equations and Dynamical Systems*; Springer-Verlag: New York, 1996.

(36) Pilling, M. J.; Seakins, P. W. *Reaction Kinetics*; Oxford University Press: Oxford, U.K., 1995.

(37) For an example where eigenvalues are explicitly defined, see Hanning-Lee, M. A.; Green, N. J. B.; Pilling, M. J.; Robertson, S. H. *J. Phys. Chem.* **1993**, *97*, 860. This case involves bimolecular terms but becomes pseudo-first order because one of the species is in excess.

(38) See, for example, the discussion in chapter 2 of ref 1.

(39) Mallard, W. G. NIST Chemical Kinetics Database, 1992 and reference cited therein.

(40) Glänzer, K.; Quack, M.; Troe, J. *Chem. Phys. Lett.* **1976**, *39*, 304.

(41) Glänzer, K.; Quack, M.; Troe J. In *Sixteenth Symposium (International) Combustion*; 1977, p 949.

(42) Hippler, H.; Luther, K.; Ravishankara, A. R.; Troe, J. *Z. Phys. Chem. NF* **1984**, *142*, 1.

(43) Slagle, I. R.; Guttman, D.; Davis, J. W.; Pilling, M. J. *J. Phys. Chem.* **1988**, *92*, 2455.

(44) Walter, D.; Grotheer, H.-H.; Davies, J. W.; Pilling, M. J.; Wagner, A. F. In *Twenty-Third Symposium (Int.) Combustion*; 1990, p 107.

(45) Hwang, S. M.; Rabinowitz, M. J.; Gardiner, W. C., Jr. *Chem. Phys. Lett.* **1993**, *205*, 157.

(46) Davidson, D. F.; DiRossa, M. D.; Chang, E. J.; Hanson, R. K.; Bowman, C. T. *Int. J. Chem. Kinet.* **1995**, *27*, 1179.

(47) Du, H.; Hessler, J. P.; Ogren, P. J. *J. Phys. Chem.* **1996**, *100*, 974.

(48) Wagner, A. F.; Wardlaw, D. M. *J. Phys. Chem.* **1988**, *92*, 2462.

(49) Smith, S. C.; Gilbert, R. G. *Int. J. Chem. Kinet.* **1988**, *20*, 307.

(50) Hessler, J. P.; Ogren, P. J. *J. Phys. Chem.* **1996**, *100*, 984.

(51) For example, eq 31 in ref 3.

(52) This form of the master equation has been used elsewhere; see ref 11 and Miller, J. A.; Klippenstein, S. J.; Robertson, S. H. *Proc. Combust. Inst.* **2000**, *28*, 1479.

(53) Expressions such as this have been used elsewhere; see, for example, ref 11.

(54) The assumption of an equilibrium constant for the master equation has been discussed in Smith, S. C.; McEwan, M. J.; Gilbert, R. G. *J. Chem. Phys.* **1989**, *90*, 4265.

(55) See, for example, Jeffrey, S. J.; Gates, K. E.; Smith, S. C. *J. Phys. Chem.* **1996**, *100*, 7090 and references therein.

(56) Frankcombe, T. J.; Smith, S. C. *Faraday Discuss.* **2001**, *119*, 159.